Hindawi
Journal of Sensors
Volume 2022, Article ID 3201104, 23 pages
https://doi.org/10.1155/2022/3201104

Research Article

Seismogenic Anomalies in Atmospheric Gravity Waves as Observed from SABER/TIMED Satellite during Large Earthquakes

Subrata Kundu,[1] **Swati Chowdhury**,[1] **Soujan Ghosh**,[1] **Sudipta Sasmal**,[1] **Dimitrios Z. Politis**,[2] **Stelios M. Potirakis**,[2] **Shih-Sian Yang**,[3] **Sandip K. Chakrabarti**,[1] **and Masashi Hayakawa**[4]

[1]*Department of Ionospheric Sciences, Indian Centre for Space Physics, 43, Chalantika, Garia Station Road, Kolkata 700084, India*
[2]*Department of Electrical and Electronics Engineering, Ancient Olive Grove Campus, University of West Attica, 12241 Egaleo, Greece*
[3]*Department of Space Science and Engineering, National Central University, Taoyuan 32001, Taiwan*
[4]*Hayakawa Institute of Seismo Electromagnetics, Co. Ltd, UEC Alliance Center, Chofu Tokyo 182-0026, Japan*

Correspondence should be addressed to Subrata Kundu; mcqmld@gmail.com

Received 11 June 2021; Revised 9 September 2021; Accepted 7 December 2021; Published 10 January 2022

Academic Editor: Giovanni Diraco

Atmospheric disturbances caused by seismic activity are a complex phenomenon. The Lithosphere–Atmosphere–Ionosphere Coupling (LAIC) mechanism gives a detailed idea to understand these processes to study the possible impacts of a forthcoming earthquake. The atmospheric gravity wave (AGW) is one of the most accurate parameters for explaining such LAIC process, where seismogenic disturbances can be explained in terms of atmospheric waves caused by temperature changes. The key goal of this work is to study the perturbation in the potential energy associated with stratospheric AGW prior to many large earthquakes. We select seven large earthquakes having Richter scale magnitudes greater than seven ($M > 7.0$) in Japan (Tohoku and Kumamoto), Mexico (Chiapas), Nepal, and the Indian Ocean region, to study the intensification of AGW using the atmospheric temperature profile as recorded from the Sounding of the Atmosphere using Broadband Emission Radiometry (SABER) satellite. We observe a significant enhancement in the potential energy of the AGW ranging from 2 to 22 days prior to different earthquakes. We examine the conditions of geomagnetic disturbances, typhoons, and thunderstorms during our study and eliminate the possible contamination due to these events.

1. Introduction

According to several research, it is well accepted that there are significant disturbances detected in the regular atmospheric processes due to seismic hazards [1–3]. A hypothetical mechanism called Lithosphere Atmosphere Ionosphere Coupling (LAIC) has been proposed to investigate and validate this strange physical mechanism that exists underneath the earth's surface and propagates up to ionospheric heights through a number of geophysical and geochemical processes. LAIC is proposed to be functional through three major channels: (a) the chemical, (b) the acoustic, and (c) the electromagnetic [3]. There are a wide variety of processes involving electromagnetic disturbances, starting from disruption in the very low frequency (VLF)/low frequency radio signals and ultralow frequency (ULF)/extreme low frequency (ELF) [4–12], changes in plasma density in higher ionospheric altitudes [13–15], irregularities in total electron content (TEC) [16–22] etc. The primary acting agent of the acoustic channel is atmospheric gravity wave (AGW) excitation, which may occur as an outcome of atmospheric oscillation in stratospheric heights above the epicenter of a similar earthquake, swaying upward, and disrupting upper atmospheric altitudes. Gravity waves (GWs) are generated as the gravitational force or buoyancy attempts to reestablish harmony in a liquid medium or at the interface of two mediums, according to fluid dynamics [23, 24]. GWs are the method for transmitting energy to the stratosphere and mesosphere from the lower atmosphere. Two of the principal factors in GW generation are frontal systems or the wind stream moving through mountains in the lower atmosphere. The momentum transfer function is as follows: first, waves spread with an almost continuous mean velocity across the atmosphere. The wave amplitude increases as you rise higher in height because of the low air density. Nonlinear force breaks the waves and transfers the momentum to the medium [25]. This energy exchange is responsible for driving some of the atmosphere's largest dynamical highlights. This GW affects stratospheric climate, temperature, and pressing factors in the lower stratosphere and is energized by convection systems, fly currents, and fronts that vary in size between a few hundred meters to a few kilometers, with a duration that falls between the Brunt Vaisala period and the inertial period [25]. Profound convective clouds can also create AGWs because of the collaboration between unsteady convective movements and the encompassing stable surroundings [25]. These waves change in scale from that of individual convective updrafts to bigger scopes characterized by coordinated convective structures [26]. Convectively created GWs can influence the middle atmosphere's momentum, can produce turbulence and mix, and can connect with the general climate to advance or smother new convection [27, 28]. The factors such as sudden stratospheric warming and meteorological events can also generate the AGW. AGW oscillations, which arise around the earthquake epicenter, cause fluctuations in temperature, pressure, ground motion, and other factors to disrupt the atmosphere. AGWs have the ability to propagate upward, causing ionosphere disruptions [7, 20]. AGW is a dispersion branch in atmospheric waves with a period of around 5 minutes to 10 hours and a wavelength ranging from ~10 meters to 1000 kilometers. Due to the viscous dissipation of the short-wave components, its wavelength increases with altitude, reaching hundreds of meters in the ionospheric D layer (between ~60 and~90 kilometers above sea level) and~10 kilometers in the F2 layer (above ~400 kilometers). These are the fastest oscillations in the atmosphere, capable of generating disturbances that can reach the ionosphere [29, 30].

2. Related Works

Several studies on the preseismic activity of AGW have already been reported over the last few decades. This section briefly describes those works. Before an earthquake, the hypothesis of atmospheric wave excitation due to seismic activity is reported by Garmash et al. [31], Linkov et al. [32], and Shalimov [33]. Numerous studies using both satellite and ground-based observations were conducted to examine the preseismic AGW activity. Between 1985 and 1989, AGW energies were investigated using the middle and upper atmosphere (MU) radar. Additionally, the observational results demonstrate that the jet stream exhibits an annual variance [34]. Later, Tsuda et al. [35] summarized the characteristics and variations of GW with height, season, and latitude from a combination of the abovementioned MU radar, two medium frequency (MF) radars, and a lidar. Tsuda et al. [36] investigated the global distribution of potential energy across mid-latitude using a global positioning system (GPS) temperature profile and observed that potential energy is higher during winter seasons. Dhaka et al. [37, 38] have used the Mesosphere-Stratosphere-Troposphere (MST) radar at Gadanki, India, to report AGW activity and its relationship with convections during Indian southwest rainfall. Miyaki et al. [39] were the first to have reported the AGW signature from subionospheric low-frequency signals and its role in the LAIC mechanism in Japan. Korepanov et al. [40] concluded that AGW can be an important parameter in the seismoionospheric study by using data on surface atmospheric pressure and magnetic field. To examine AGW-related potential energy (E_p), Zhang et al. [41] analyzed the temperature data from the Sounding of the Atmosphere Using Broadband Emission Radiometry (SABER) instrument installed on the Thermosphere Ionosphere Mesosphere Energetics and Dynamics (TIMED) satellite. Nakamura et al. [42] have performed a comparative investigation and attempted to track down the relating seismogenic effect for a few earthquakes. For the 2004 Niigata-Chuetsu earthquake ($M = 6.8$), wavelet analysis of those parameters reveals modifications over a period of 10 to 100 minutes, which is consistent with AGW. Using nighttime VLF fluctuation and the SABER temperature profile, previously AGW activities were investigated prior to the Imphal earthquake. Around a week before this earthquake, a large increase in E_p linked to the AGW was seen near the epicenter [43]. Piersanti et al. [20] observed enhanced AGW activity on the day of the 2018 Bayan earthquake computed from ERA5 data and also found anomalous activity in GPS-TEC on the same day. Carbone et al. [29] used a mathematical model lithosphere–atmosphere coupling for seismic events to compute vertical atmospheric temperature profile and compared the obtained results with observation. Sasmal et al. [22] found abnormal AGW activity 6 days before the 2020 Samos earthquake using the SABER temperature profile and 11 days prior to the earthquake using wavelet analysis of GNSS-TEC. Previously, Ouzounov et al. [44] used ground- and space-based observation to investigate the preseismic anomaly. The majority of the research are based on the LAIC mechanism. The data from outgoing longwave radiation (OLR), GPS-TEC, and foF2 are employed in the research. In OLR data, a large amount of radiation was emitted on March 7, an anomalous increase in TEC was seen on March 8, and abnormalities in f0F2 were recorded between March 03 and 11, 2011. For the 2011 Tohoku earthquake, Ohta et al. [45] used the Chubu University ULF/ELF network to investigate ULF/ELF electromagnetic radiation. On March 6, 2011, before the earthquake, ULF/ELF atmospheric radiation was detected. Two days before this earthquake, Sasmal et al. [46] noticed a significant shift in the sunrise terminator time (SRT) in the JJI-IERCOO path VLF signal. Using China's magnetometer data, Schekotov et al. [47] investigated ULF/ELF atmospheric radiation. The ULF/ELF atmospheric radiation had a strong signal on March 08, 2011, three days before the mainshock. Before this earthquake, Ghosh et al. [48] noticed a shift in VLF-SRT from March 8 to 11, 2011. Yang et al. [39] also investigated the generation of AGW for an oceanic 2011 Tohoku earthquake and compared it to the 2016 Kumamoto earthquake using ERA5 and SABER temperature results. The study of Yang et al. [49] discovered suspicious AGW activity four to eight days prior to the earthquake. In this scenario, the potential energy extends in the direction of the east. Chakraborty et al. [50] observed a significant shift in sunrise and sunset terminator time (SST) 3 to 4 days prior to the second Nepal earthquake (May 12, 2015). Chakraborty et al. [9] detected anomalies in the Eddy field OLR curves 3 days before the Nepal earthquakes. The increased activity of AGWs was also detected 4 days before the earthquakes utilizing the fast Fourier transform (FFT) and wavelet analysis of the JJI-IERCOO VLF signal. Ghosh et al. [48] observed a significant shift in VLF-SRT 1 day before the second Nepal earthquake. Shah et al. [51] noticed a substantial increase in land surface temperature (LST) five days before the occurrence of the first Nepal earthquake (April 25, 2015). Thermal abnormalities were seen going along the fault line on April 19 and 20, 2015, prior to the earthquake. Yang et al. [52] used ERA5 temperature profile data to report on the AGW hypothesis as an earthquake precursor. This research detected that potential energy (Ep) increased 4 to 7 days prior to the 2016 Kumamoto earthquake and eventually spread to the eastern Japan area. Hu et al. [53] observed an unusual ionospheric disturbance in TEC on the day of the Kumamoto earthquake. For the 2017 Chiapas earthquake, Stanica et al. [54] found an abnormality in the ULF geomagnetic signal from September 7 to 9, 2017. Shi et al. [55] observed unusual anomalies in the global ionospheric map (GIM) TEC 5 days prior to the same earthquake.

It is clear that there are lots of precursory studies already presented for the Tohoku earthquake (March 11, 2011), Indian Ocean earthquake (April 11, 2012), Nepal earthquakes (April 25, 2015, and May 12, 2015), Kumamoto earthquake (April 15, 2016), and Chiapas earthquake (September 08, 2017) in various channels of LAIC mechanism. So, it is interesting to see the effect of these abovementioned earthquakes in the acoustic channel. This paper presents a detailed analysis of AGW activity in the stratosphere using SABER temperature profile for the specific earthquakes. The detailed analysis of this work is presented in Section 2. The findings of this research are presented in Section 3. Finally, the concluding remarks are presented in Section 4.

3. Materials and Methods

According to United States Geological Survey (USGS) (https://earthquake.usgs.gov/), the earthquakes are classified into seven different classes according to their magnitude. Based on this classification, the earthquake magnitudes (M) between 7.0 and 7.9 are classified to the "major earthquake" class, while $M \geq 8$ earthquakes are classified to the "great earthquake" class. Therefore, the studied 2011 Tohoku earthquake ($M = 9$), 2012 Indian Ocean earthquakes ($M = 8.6$ and 8.3), and 2017 Chiapas earthquake are great earthquakes, while Nepal earthquakes ($M = 7.8$ and 7.3) and Kumamoto earthquake ($M = 7$) are major earthquakes. The abovementioned earthquakes were chosen to study the AGW activity. The general information of the earthquakes as collected from USGS are presented in Table 1. Each earthquake's seismic preparation zone was calculated using Dobrovolsky's radius equation. The equation provides the radius of a circle representing the preparation zone of the earthquake as: $R = 10^{0.43M}$, where M is the magnitude of the earthquake. The epicenter of the earthquake is situated at the center of the circle [56]. The preparation zone of each one of the studied earthquakes is presented in Table 1 and shown in Figure 1.

The Tohoku earthquake happened near the coast of Japan at 14 : 46 Japan Standard Time (JST) (05 : 46 UTC) on March 11, 2011. The epicenter was situated at roughly 70 km east of the Oshika Peninsula of Tohoku (geographic coordinates: 38.297°N, 142.372°E) with an underwater depth of approximately 29 km. The magnitude of the earthquake was $M = 9.0$. The magnitudes of the Indian Ocean earthquakes on April 11, 2012, were $M = 8.6$ and $M = 8.2$, respectively. At 08 : 38 UTC on April 11, 2012, the earthquake epicenter was about 610 kilometers southwest of Banda Aceh (geographic coordinates: 2.327°N, 93.063°E) in Indonesia, with a depth of 22.9 kilometers. At 10 : 43 UTC, two hours after the first earthquake, an aftershock of magnitude $M = 8.2$ struck at a depth of 16.4 km about 430 km southwest of Banda Aceh (geographic coordinates: 0.802°N, 92.463°E). In the year 2015, Nepal was hit by two earthquakes. On April 25, 2015, a magnitude $M = 7.8$ earthquake struck at 11 : 56 Nepal Standard Time (NST), or 6 : 11 UTC. With a depth of 8.2 km, the epicenter was situated east of Gorkha District at Barpak, Gorkha (geographic coordinates: 28.23°N, 84.731°E). On May 12, 2015, at 12 : 50 p.m. local time, Nepal's second earthquake struck (07 : 05 UTC). The epicenter was 18 kilometers deep and located on the frontier of the Nepalese districts of Dolakha and Sindhupalchowk (geographic coordinates: 27.837°N, 86.077°E). The earthquake measured $M = 7.3$ in magnitude. The Kumamoto earthquake happened in central Kyushu (geographic coordinates: 32.793°N, 130.749°E), Japan at 01 : 25 JST on April 16, 2016 (16 : 25 UTC on April 15) with a depth of 10 km. The main shock of the earthquake had a magnitude of $M = 7.0$, and the fore shock had a magnitude of $M = 6.2$, all of which occurred on April 14, 2016.The Chiapas earthquake happened in the Gulf of Tehuantepec off the southern coast of Mexico, near the state of Chiapas (geographic coordinates: 15.022°N, 93.899°W), approximately 87 km southwest of Pijijiapan with a magnitude of $M = 8.2$ at 4 : 49 UTC on September 8, 2017 (local time: 23 : 49 CDT, September 7, 2017) with a depth of 50 km.

To avoid possible contamination of the atmosphere due to solar geomagnetic storms, the geomagnetic situation is studied for ±30 days from the day of earthquake. D_{st} and K_P are the main geomagnetic indices during such period

Table 1: Earthquake details.

Date	Epicenter latitude	Epicenter longitude	Magnitude (M)	Preparation zone (km)	Epicenter location	Country
11-03-2011	38.297	142.372	9.1	8185	Tohoku	Japan
11-04-2012	2.327	93.063	8.6	4989	Indian Ocean	Indo-Australian Plate
11-04-2012	0.802	92.463	8.2	3357	Indian Ocean	Indo-Australian Plate
25-04-2015	28.147	84.708	7.8	2259	Gorkha	Nepal
12-05-2015	27.837	86.077	7.3	1377	Gorkha	Nepal
15-04-2016	32.793	130.749	7	1023	Kumamoto	Japan
08-09-2017	15.022	-93.899	8.2	3357	Chiapas	Mexico

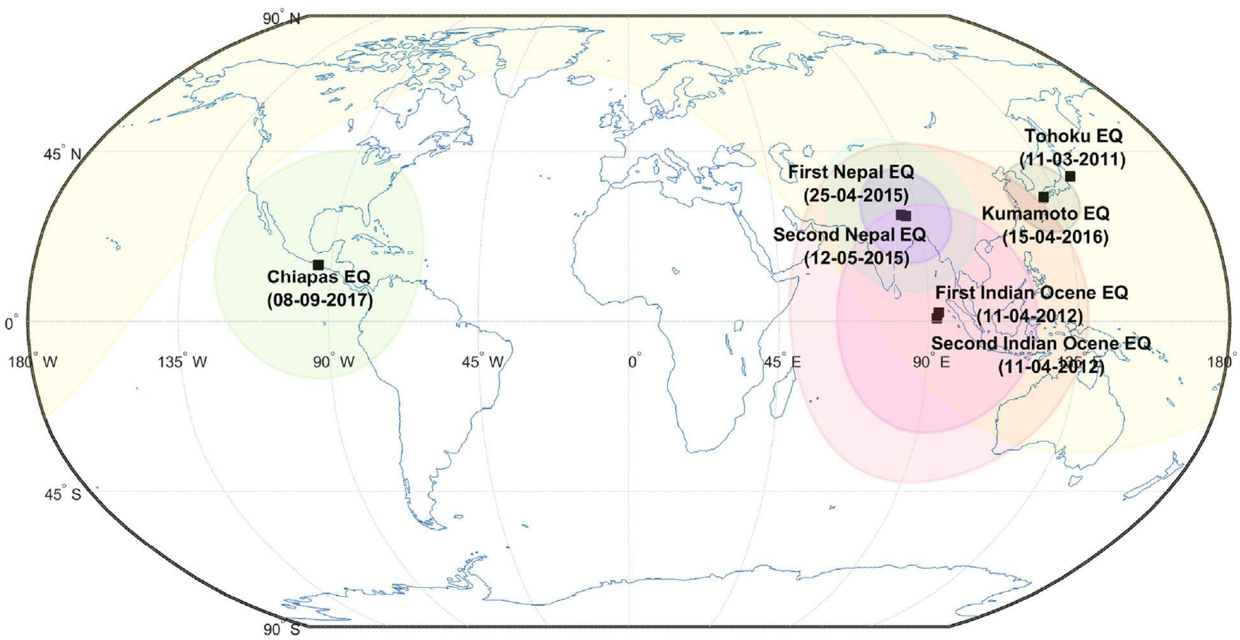

Figure 1: The epicenters of the studied earthquakes are marked along with the corresponding earthquake preparation zones (Dobrovolsky's radius) on the world map. The black solid squares represent the epicenters of the earthquakes. The preparation zones of the Tohoku, first and second Indian Ocean, first and second Nepal, Kumamoto, Chiapas earthquakes are represented by yellow, red, magenta, cyan, blue, black, and green colors, respectively.

for individual earthquake is shown in Figure 2. The geomagnetic data (Kp and, D_{st}) are taken from OMNIWEB NASA archive (https://omniweb.gsfc.nasa.gov/). Figures 2(a) and 2(g) show that three mild geomagnetic storms were detected during the Tohoku earthquake on February 14, March 1, and March 11, 2011. The first geomagnetic storm occurred 24 days before the earthquake with a minimum D_{st} value of -40 nT and a maximum Kp value of 5.3. The earthquake occurred 10 days after the second geomagnetic storm. For the specific geomagnetic storm, the D_{st} has a minimum value of -88 nT, and the maximum value of Kp is 5.3 for this storm. On the earthquake day, there was a third geomagnetic storm. D_{st} lowest value was -83 nT, and the highest value of Kp was 5.3. Figure 2(b) shows that the D_{st} reached a minimum value of -60 nT on April 5, 2012, which is six days before the earthquake and a second minimum value of -60 nT on April 13, 2012, which is two days after the earthquake. As seen in Figure 2(h), the maximum value of Kp is 4.0 and 4.3, which is less than 5.0, indicating that both storms are minor. Therefore, the preearthquake period was quiet for the Indian Ocean earthquake. Again, the minimum value of D_{st} for the storm that happened 14 days after the earthquake was -120 nT. For this storm, the maximum value of K_P is 5.7. Figures 2(c) and 2(i) and Figures 2(d) and 2(j) reveal that the seven days prior to both earthquakes were geomagnetically quiet for the Nepal earthquake. Figures 2(c) and 2(i) reveal that the D_{st} drops to a minimum of -79 nT on April 16, 2015, 9 days before the earthquake, and the Kp reaches a limit of about 4.0. On May 13, 2015, just one day after the earthquake, the D_{st} hits its lowest value of -76 nT, and the highest Kp value is 5.7 as observed from Figures 2(d) and 2(j). The D_{st} value for the Kumamoto earthquake was -60 nT on April 8, 2015 (7 days prior to the earthquake), and the Kp value was 5.7. On the earthquake day, April 15, 2016, another minor storm occurred (see Figures 2(e) and 2(k)) with a minimum D_{st} value of

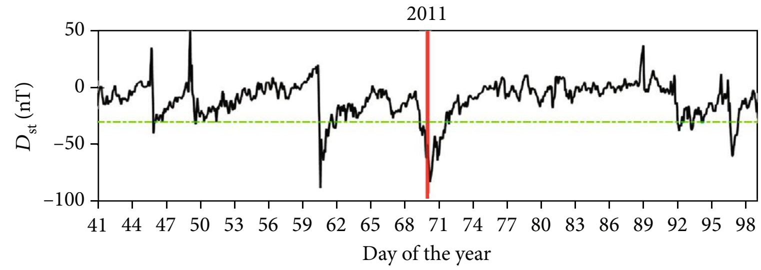

(a) 2011

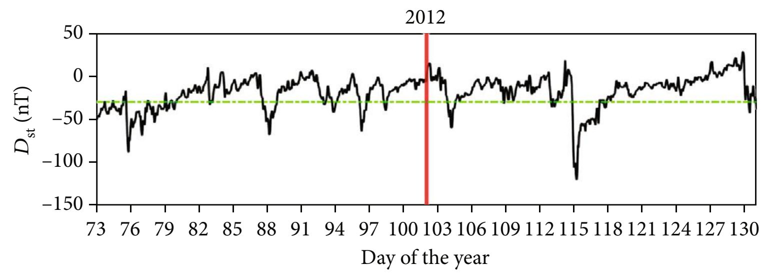

(b) 2012

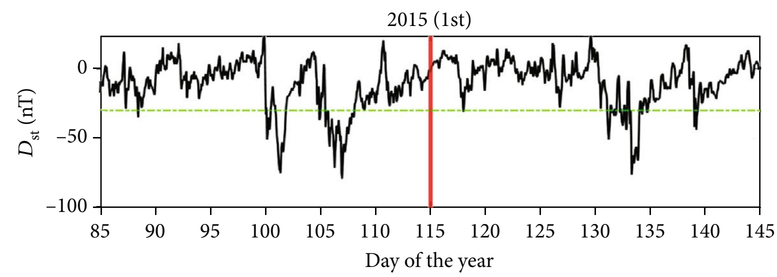

(c) 2015 (1st)

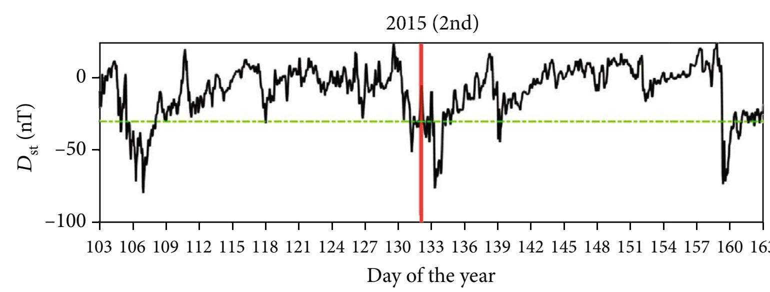

(d) 2015 (2nd)

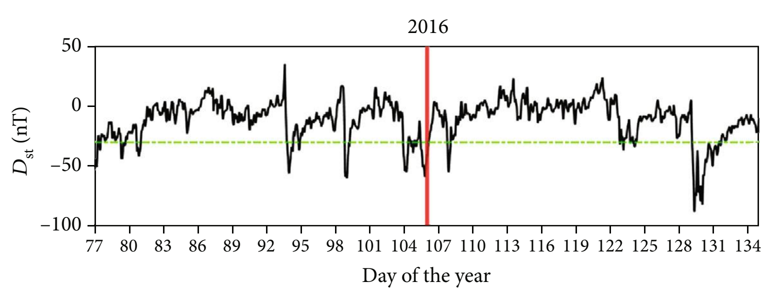

(e) 2016

Figure 2: Continued.

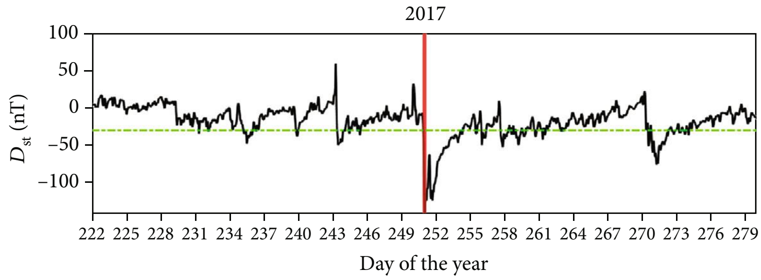

(f) 2017

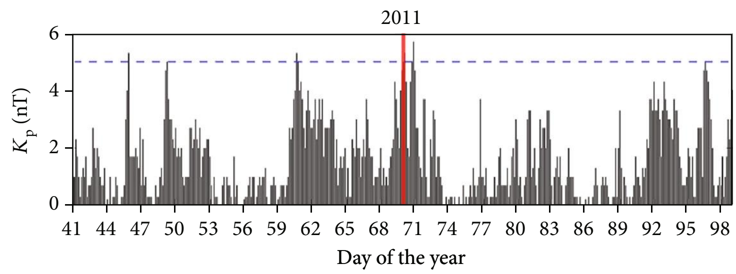

(g) 2011

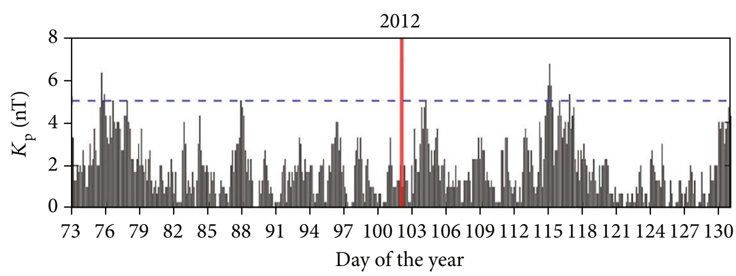

(h) 2012

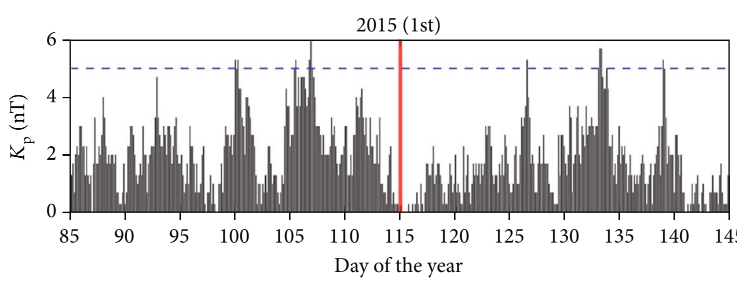

(i) 2015 (1st)

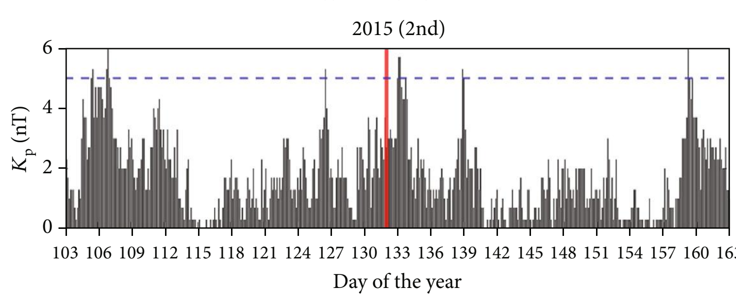

(j) 2015 (2nd)

Figure 2: Continued.

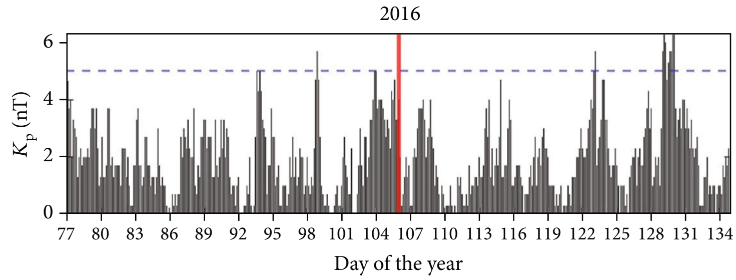

(k) 2016

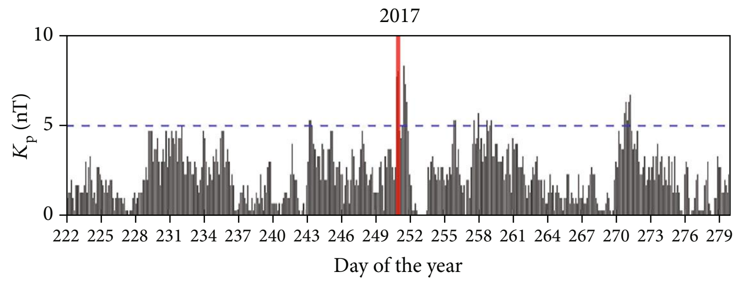

(l) 2017

Figure 2: The variation of geomagnetic indices during the period of earthquakes period. The left side panels present the geomagnetic D_{st}, while the right side panels present the K_P index. In (a) and (g), the geomagnetic indices D_{st} and Kp for the 2011 Tohoku earthquake are presented. The red vertical line indicates the earthquake day. Similarly, in (b)-(h), (c)-(i), (d)-(j), and (e)-(k) and (f)-(l), the same are presented for the Indian Ocean, first Nepal, second Nepal, Kumamoto, and Chiapas earthquakes, respectively, and the green and blue horizontal dashed are represented threshold value of an occurrence of a storm.

-60 nT and a maximum Kp value of 43. A strong geomagnetic storm occurred on the day of the Chiapas earthquake, as shown in Figures 2(f) and 2(l). The lowest D_{st} value was -142 nT, and the highest Kp value was 8.3. Minor storms with a minimum D_{st} value of -50 nT and a maximum Kp value of 4.3 occurred 15 days prior to the earthquake.

3.1. SABER/TIMED Temperature profile. On December 7, 2001, the TIMED satellite was launched into a 625 km orbit with a 74.1° inclination. The period of the satellite is 1.7 hours [57]. Four instruments make up the TIMED satellite. Global Ultraviolet Imager (GUVI), SABER, Solar Extreme Ultraviolet Experiment (SEE), and TIMED Doppler Interferometer (TIDI) are the instruments [58]. Out of these four instruments, this study deals with the SABER part. It obtains the ambient temperature profile of an altitude range of 20 to 110 km using a wavelength ranging from 1.27 to 1.7 μm. In northward viewing, SABER's latitudinal coverage ranges from 50°S to -82°N, and in southward viewing, it ranges from 50°N to -82°S. After every 60 days of a cycle, it updates the observation coverage. It primarily covers the latitudinal range of 50°S to -50°N on average. The methodology to obtain the temperature profile has been discussed by Remsbarg et al. [59] by using SABER. As the SABER is a limb sounding infrared radiometer, the previous reports have shown that AGWs with horizontal and vertical wavelengths (λ_Z) longer than 100 to 200 km and 4 km, respectively, can be observed [60].

3.2. Calculation of the Atmospheric Gravity Waves (AGWs). The method for analyzing AGW has already been developed by Fetzer et al. [61] and Preusse et al. [60, 62]. The method of analysis has also been used to analyze the AGW by Piersanti et al. [20], Sasmal et al. [22], Biswas et al. [43], Yang et al. [49, 52], Suhai et al. [58], Yan et al. [63], Yamashita et al. [64], Thurairajah et al. [65], Yang et al. [66], and Liu et al. [67, 68]. There are several measures involved in extracting AGW from a temperature profile. The temperature (T) profile for a specific geographic area with a finite latitude/longitude range is first retrieved from the SABER archive data (http://saber.gats-inc.com/). The logarithm of each individual temperature profile is then computed. Fitted values are derived from the logarithmic temperature using a third-degree polynomial. The residual values are then derived by subtracting the fitted temperature profile from the initial profile. A 4 km boxcar filter is added to the residual values to remove other waves of wavelength shorter than 4 km. The final profile is computed by combining the filtered residual values with the fitted value. The least square fit (LSF) of these profiles is the antilogarithm. The regular zonal mean temperature and other zonal wave components are calculated using these LSFs, ranging from 1 to 5. The number of all wave components from 0 to 5 is the background temperature (T_0). By subtracting the background temperature from the initial profiles, the perturbation temperature (T_p) is obtained. By putting the values into equation (1), the potential energy (E_p) associated with the AGW is derived.

$$E_p = \frac{1}{2}\left(\frac{g}{N}\right)^2\left(\frac{T_p}{T_0}\right)^2, \tag{1}$$

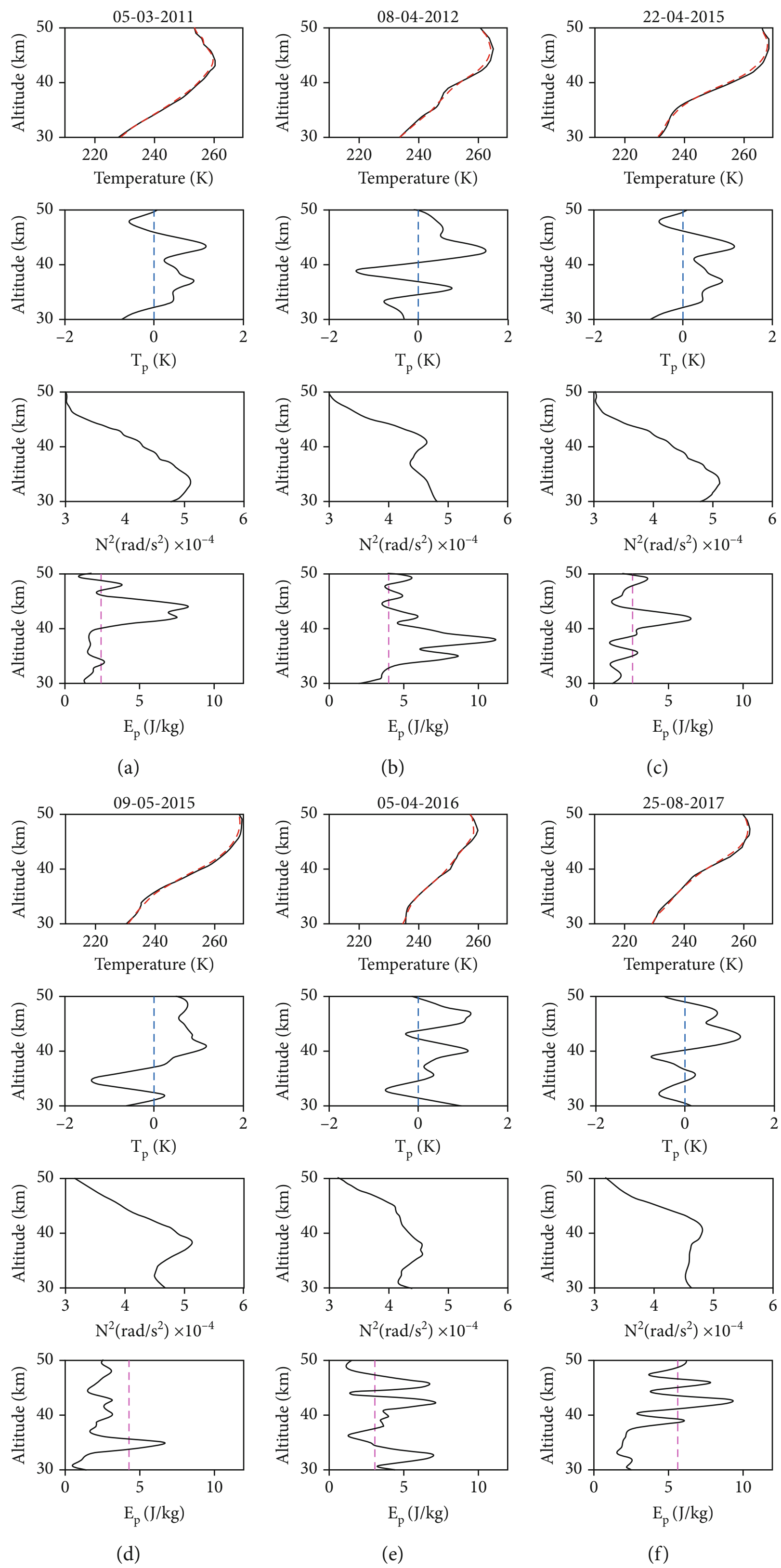

Figure 3: Altitude variation of temperature in Kelvin (black solid curve) with 3rd order polynomial fitted value (red dashed curve), perturbation temperature T_p (solid black curve) and the nonperturbed temperature (blue dashed line), Brunt Vaisala Frequency N^2 in rad/S^2, calculated potential energy E_p in J/kg, and threshold E_p (magenta dotted line) from 30 to 50 km on: (a) 05-03-2011, for Tohoku earthquake, (b) 08-04-2012, for Indian Ocean earthquake, (c) 22-04-2015, for first Nepal earthquake, (d) 09-05-2015 for second Nepal earthquake, (e) 05-04-2016 for Kumamoto earthquake, and (f) 25-08-2017 for Chiapas earthquake.

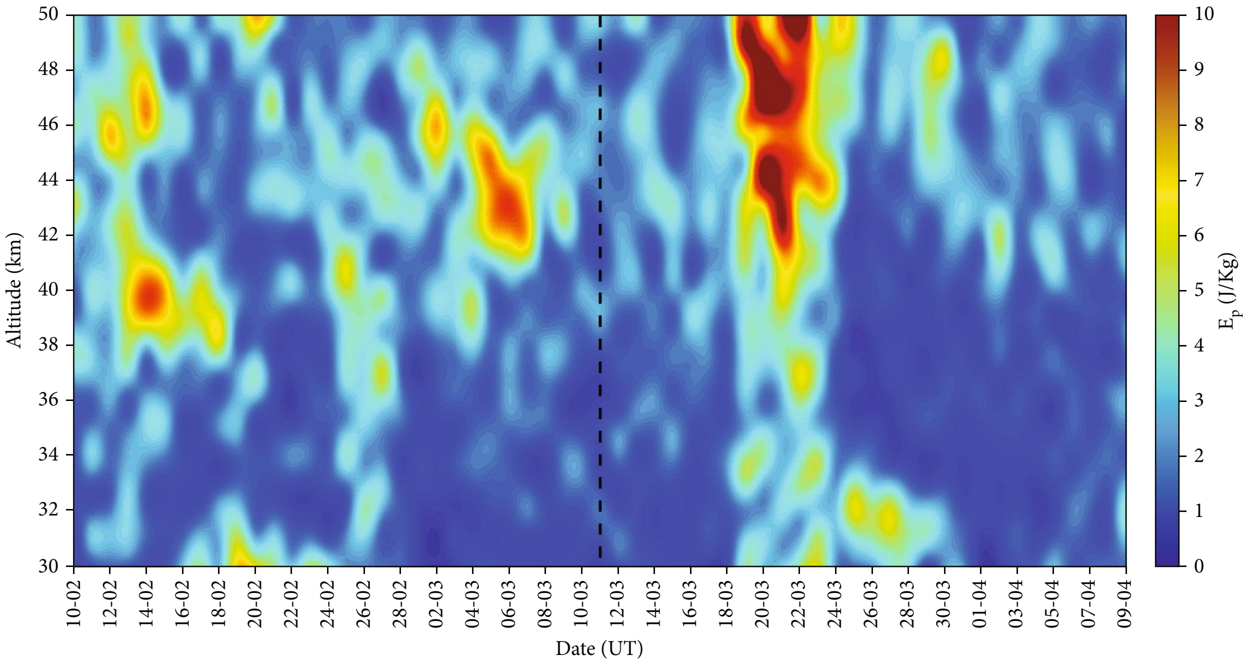

Figure 4: Potential energy variation during February 10 to April 9, 2011, for the Tohoku earthquake. X and Y axes indicate the date (UT) and altitude (km), respectively. The color bar indicates the E_p in J/kg. The black dashed line indicates the earthquake day.

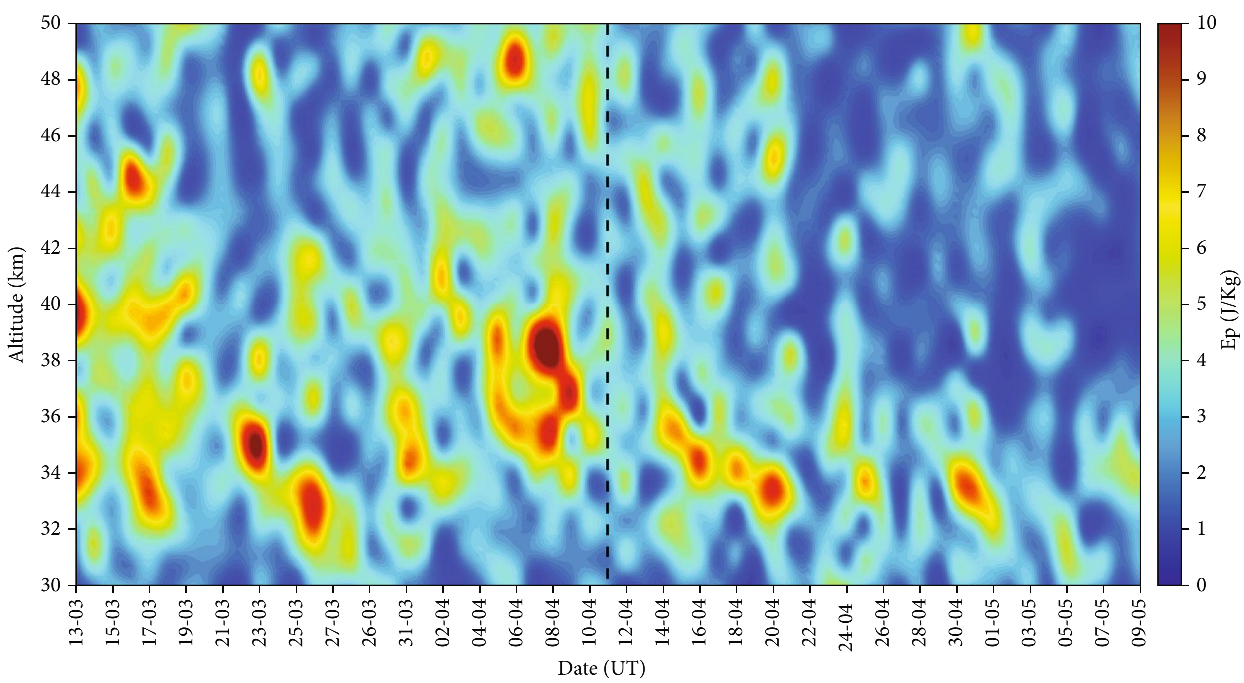

Figure 5: Same as Figure 4 from March 13 to May 10, 2012 for the Indian Ocean earthquake.

where g denotes gravity's acceleration, and N denotes the Brunt–Väisälä frequency described by

$$N^2 = \frac{g}{T_0}\left(\frac{\partial T_0}{\partial z} + \frac{g}{c_p}\right). \tag{2}$$

Here, z is the altitude, and c_p is the specific heat at constant pressure.

A nine-dimensional matrix is generated after the computation of E_p. Latitude, longitude, date or day of the year in UT, altitude, original SABER temperature profile, reconstructed fitted temperature profile, perturbation

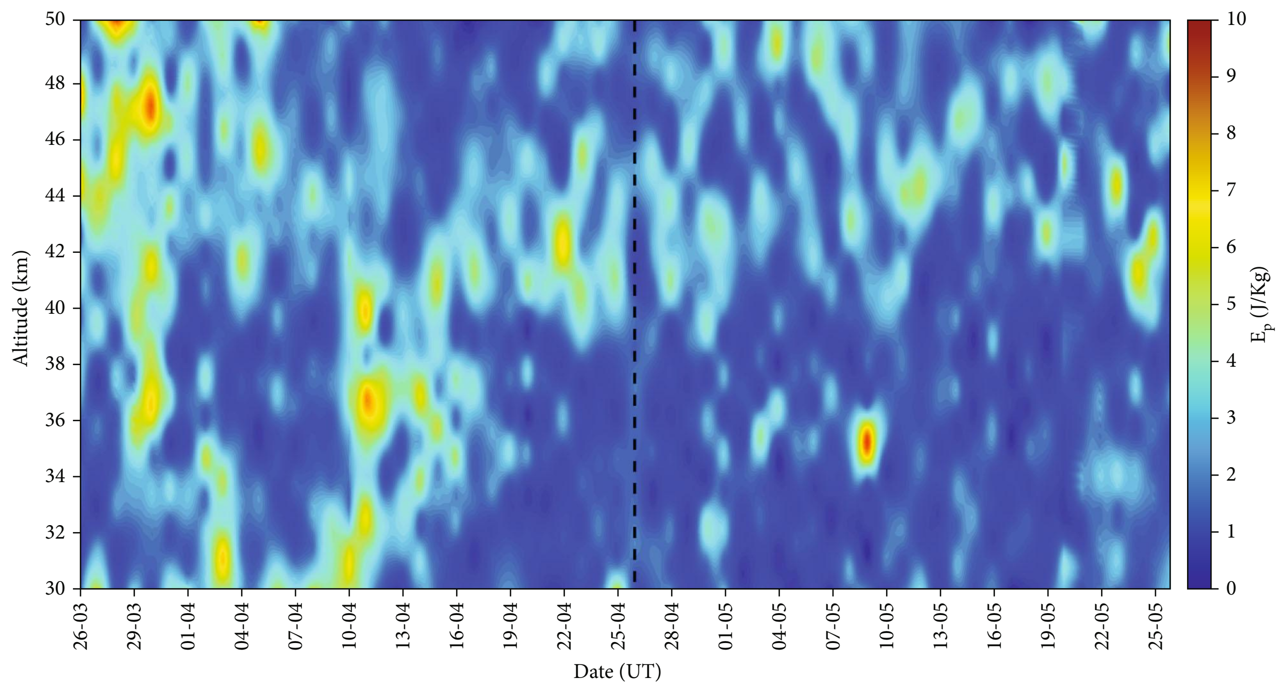

Figure 6: Same as Figure 4 for the period of March 26, 2015 to May 25, 2015 for the first Nepal earthquake.

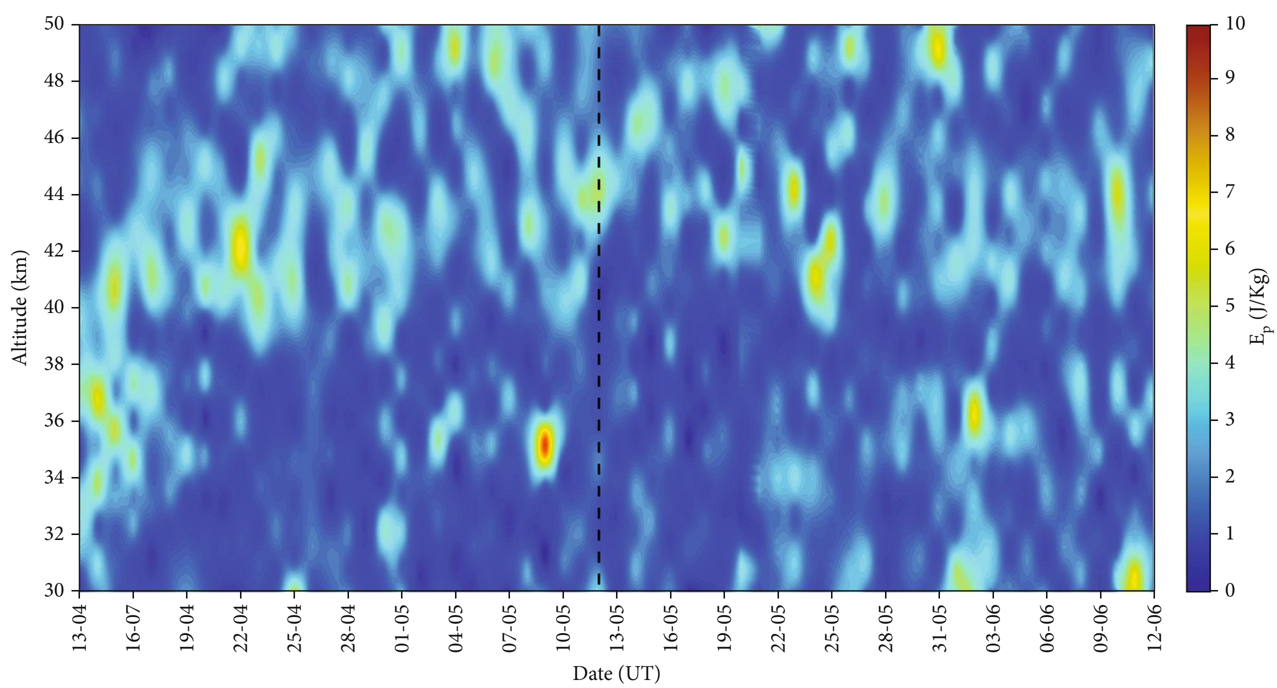

Figure 7: Same as Figure 4 for the period of April, 13 to June 12, 2015 for the second Nepal earthquake.

temperature, Brunt–Väisälä frequency, and AGW-related potential energy (E_p) are all part of this nine-dimensional matrix. A specific area for the various earthquakes is initially selected to evaluate the possible generated AGW connected with earthquakes. The geographic area is chosen from 20°N to 60°N, 120°E to 160°E and the time from February 10 to April 9, 2011, for the Tohoku earthquake. Similarly for the Indian Ocean earthquake from February 13 to May 10, 2012, from 15°S to 10°N and 70°E to 110°E, The chosen area for spatial distribution is from 20°N to 40°N and 70°E to 110°E for the two Nepal earthquakes in 2015, from March 26, 2015, to May 25, 2015 (first Nepal earthquake) and April

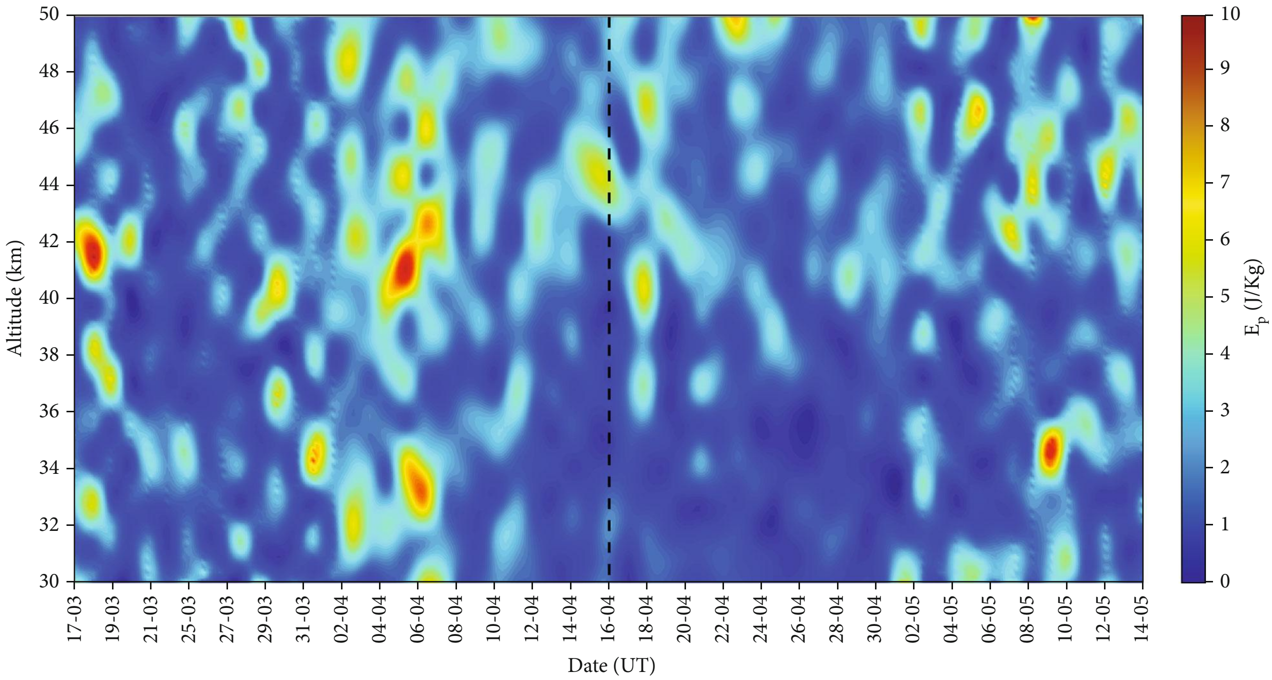

FIGURE 8: Same as Figure 4 from March 17 to May 14, 2016 for the Kumamoto earthquake.

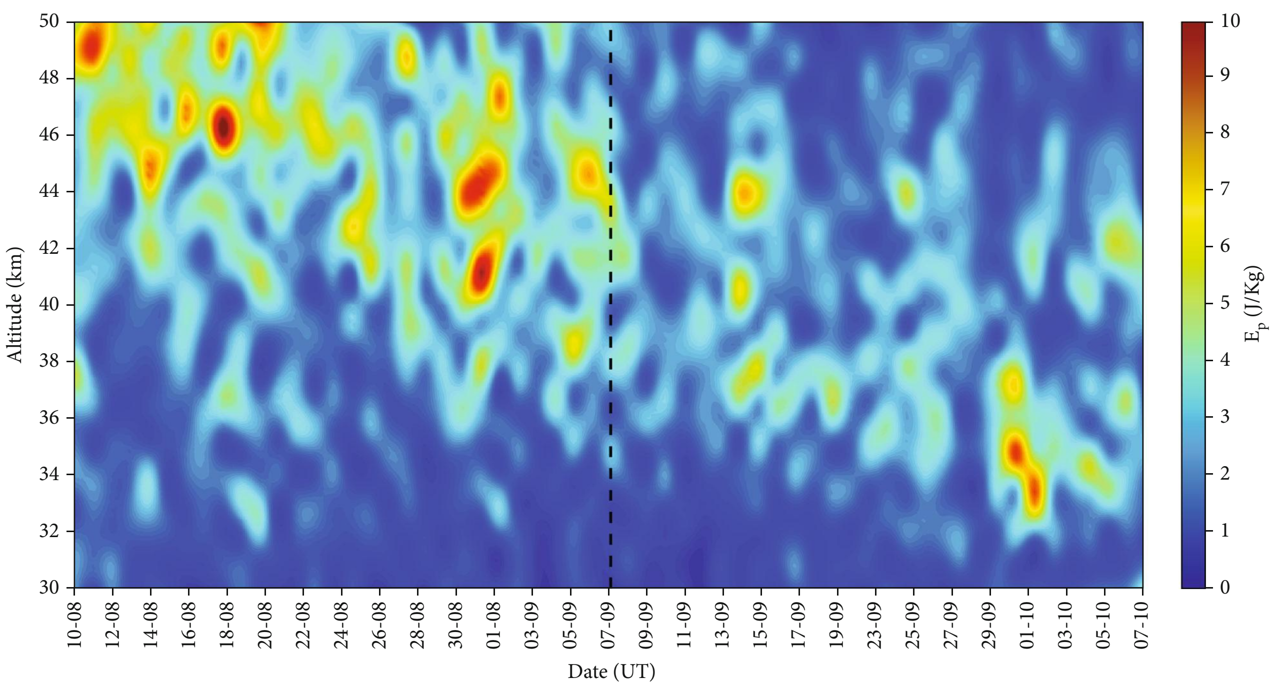

FIGURE 9: Same as Figure 4 for the period of August 10 to October 7, 2017 for the Chiapas earthquake.

13 to June 12, 2015 (second Nepal earthquake). The spatial area 15°N to 40°N and 120°E to 140°E is used for the Kumamoto earthquake from March 17 to May 14, 2016. Finally, the geographic area for the Chiapas earthquake (2017) is 5°S to 25°N and 70°W to 110°W from August 10, 2017, to October 7, 2017. For all of the earthquakes, the height range is 30 to 50 km. The variations in background potential energy (E_p) were estimated using Yang et al. [49, 52, 66] approach. In this study, the computation of the E_p at various altitudes for the same region and time period were

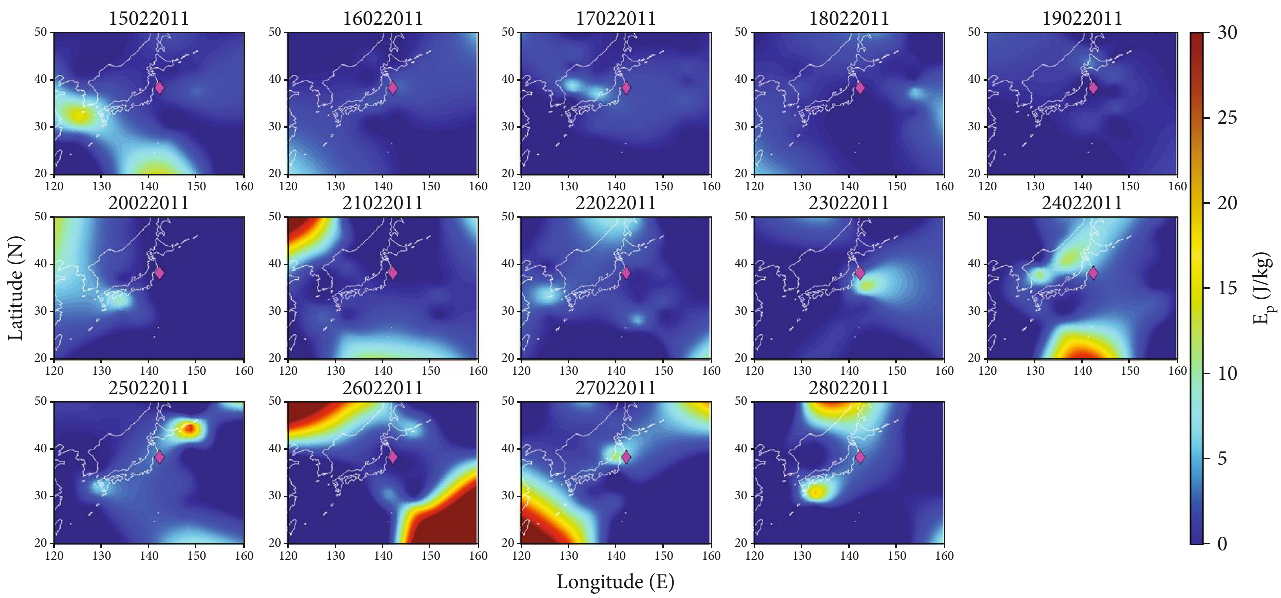

FIGURE 10: Spatial variation of potential energy at an altitude of 43 km from February 15 to 28, 2011 for Tohoku earthquake 2011. X axis and Y axis represent the longitude and latitude, respectively. The magenta diamond represents the earthquake epicenter, and the white lines indicate the country border. The numbers appearing on top of each subplot denote the corresponding day in the following format: "DDMMYYY," where D, M, and Y are digits of the day, month, and year, respectively. For example, "01032011" means March 1, 2011.

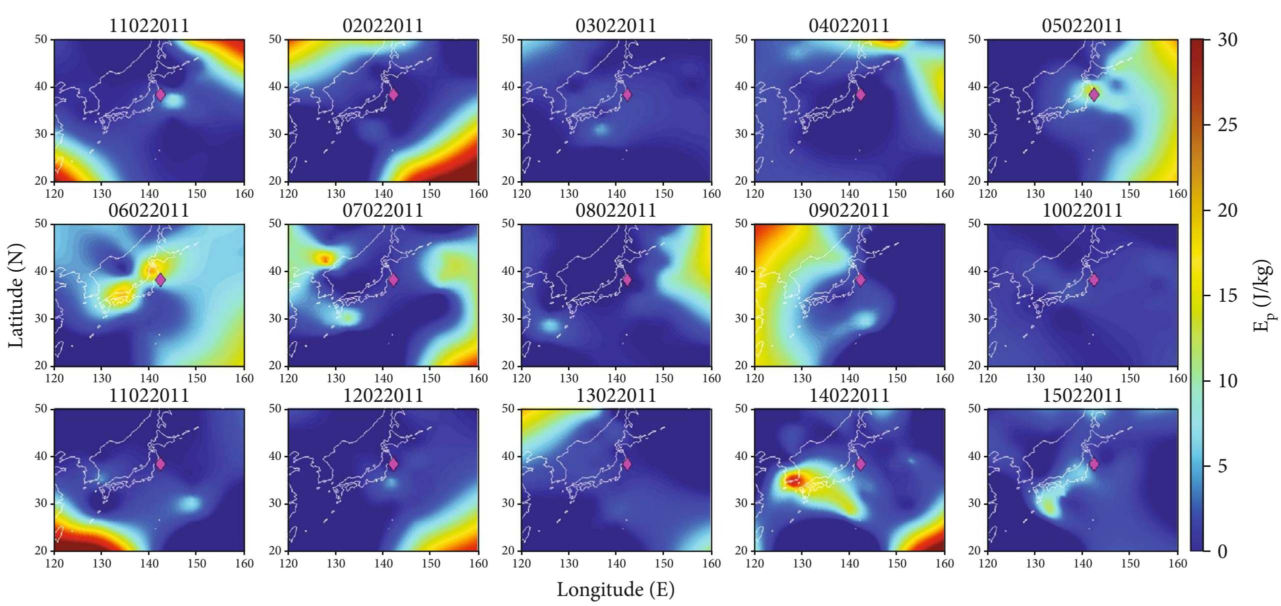

FIGURE 11: Same as Figure 10 during March 1 to 15, 2011 at 44 km altitude.

used to determine background changes. Three years preceding the earthquake year were used for this calculation. At various altitudes, the recorded E_p values differ. The average of E_p corresponding to the three years was used to determine the E_p background threshold value. If the E_p value of any day in the ± 15 days period from the day of the earthquake exceeds the threshold value, then this day is considered to be an anomalous day possibly associated with the specific earthquake. It is worth noting that any anomalous day observed by this method must have been geomagnetically and meteorologically quiet. All the metalogical conditions around the earthquake period were gathered from Japan Meteorological Agency (JMA) (http://www.jma.go.jp/jma/index.html), Bureau of Meteorology (Australian Government) (http://www.bom.gov.au), Indian Meteorological Department (IMD) (https://metnet.imd.gov.in/imdnews/), joint collaboration of National

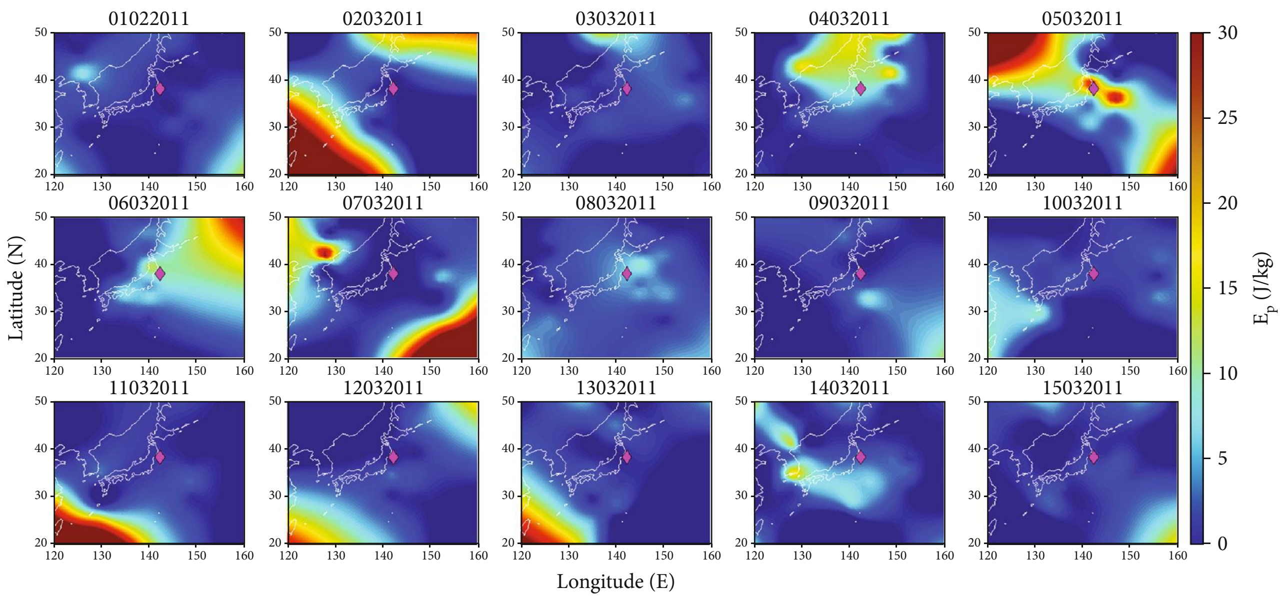

FIGURE 12: Same as Figure 10 during March 1 to 15 at 43 km altitude.

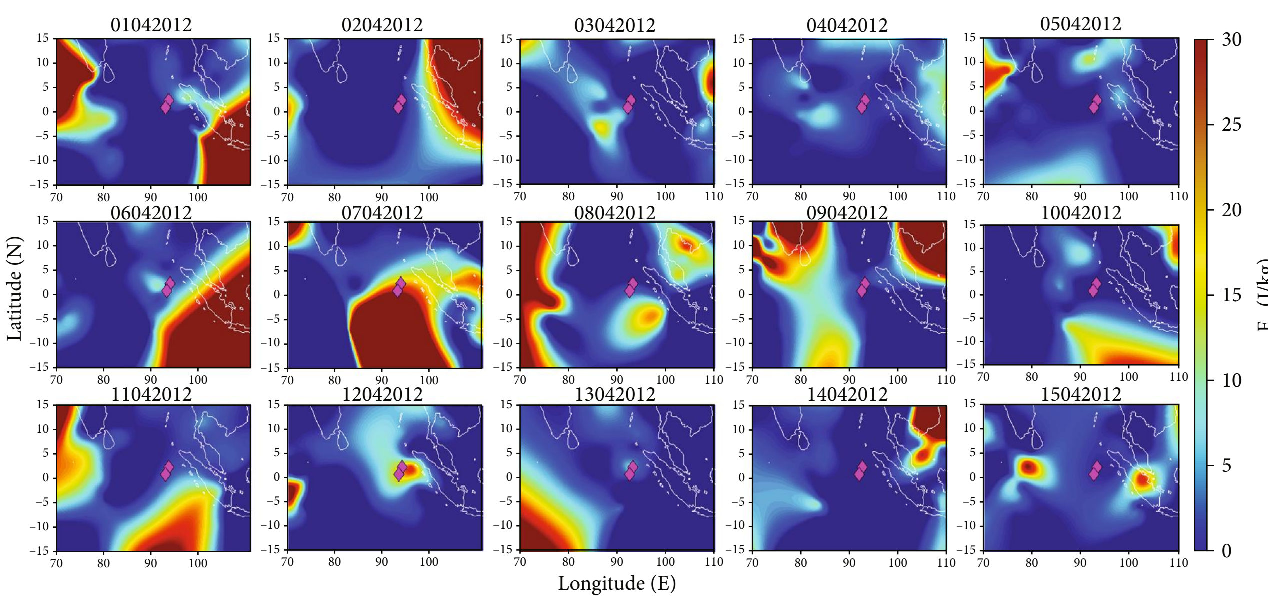

FIGURE 13: Spatial variation of potential energy at 34 km altitude from April 1 to 15, 2012 for the Indian Ocean earthquake.

weather service (NWS), and National Oceanic and Atmospheric Administration (NOAA) (https://www.nhc.noaa.gov/data/tcr/).

4. Results

4.1. Altitude variation of AGWs. A nine-dimensional matrix provides the altitude profile of real temperature along with reconstructed fitted profile, perturbation temperature, Brunt Vaisala frequency, and E_p associated with AGW. As it is already mentioned in the materials and method part (section 2.2), the anomalous days were identified as those exceeding the threshold E_p value for each earthquake. Based on this, for the Tohoku earthquake, the threshold value of E_p is 2.372 J/kg at 44 km altitude. For this earthquake on March 5, 2011, the value of E_p is about 8.3 J/kg at the same altitude, which is the maximum exceeding the threshold. Similarly, the threshold value for the Indian Ocean earthquake is 4 J/kg, and on April 8, 2012, the E_p crosses this value at 38 km. The maximum value of E_p is around 11 J/kg. In the case of the two earthquakes that struck Nepal in 2015, the anomalous days are April 22 and May 9, 2015, in which the maximum values of E_p are 6.6 J/kg at 35 km and 6.5 J/kg at 42 km, respectively. The corresponding threshold values for these two earthquakes are 2.6 J/kg and 4.2 J/kg, respectively. For the Kumamoto earthquake, the anomalous

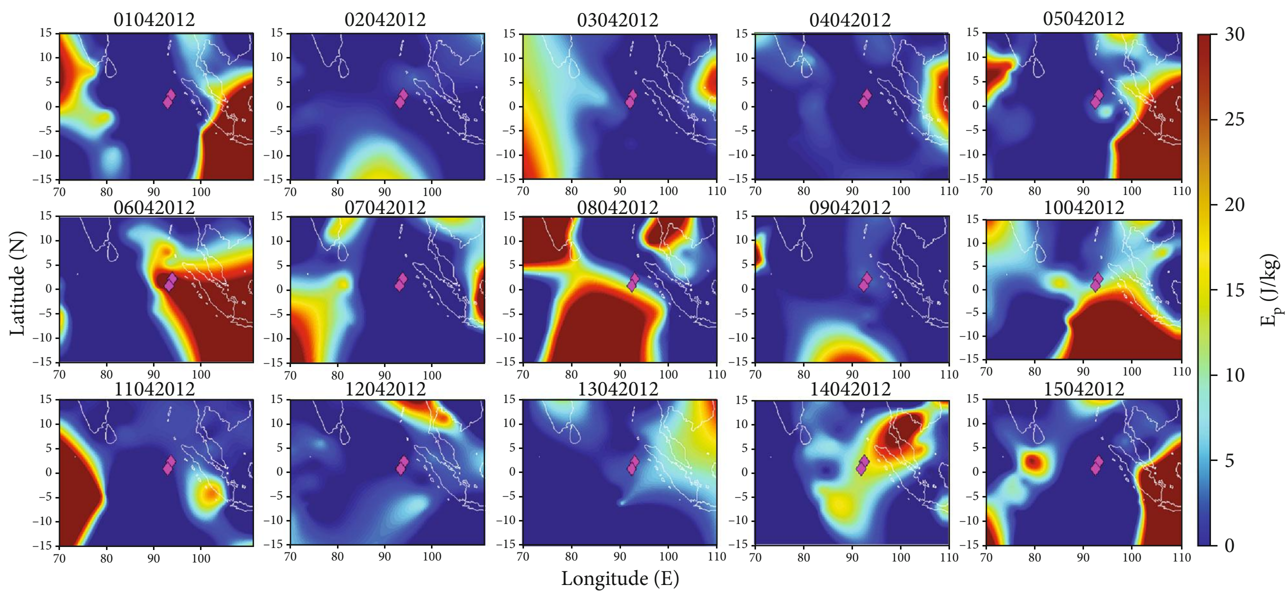

FIGURE 14: Same as Figure 13 at 35 km altitude.

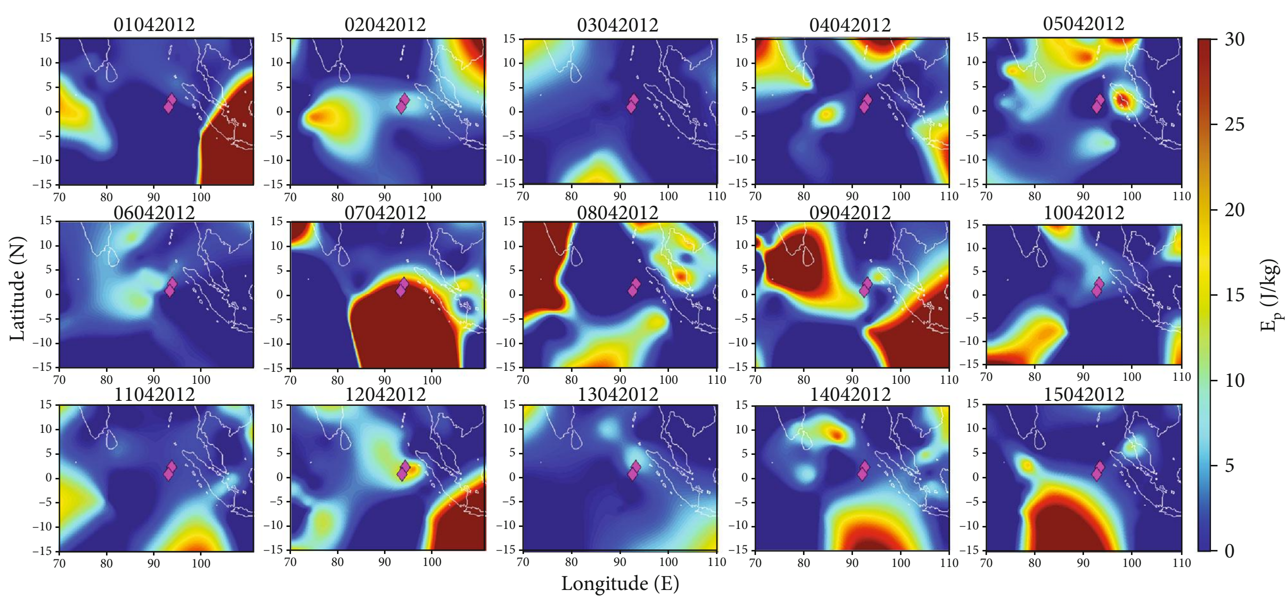

FIGURE 15: Same as Figure 13 at 37 km altitude.

day is identified on April 5, 2016. The maximum and threshold value of E_p for the specific earthquake is 7.2 J/kg and 3.06 J/kg, respectively, at 42 km altitude. The highest E_p value for the Chiapas earthquake is about 9.3 J/kg at 42 km on August 25, 2017, with the threshold value 5.6 J/kg. All the E_p variations for the identified anomalous days are presented in Figure 3.

The time altitude variation of E_p associated with AGW is computed from the nine-dimensional matrix for the above-mentioned earthquakes, and the three-dimensional profile of such E_p variation is presented in Figures 4–9. The X-axis shows the dates (in UT) around the earthquakes, and Y-axis represents the altitude profiles in km the color bars show the E_p in J/kg. For the Tohoku earthquake, Figure 9 shows a significant increment in E_p that occurred around 43 km from March 5 to 7, 2011, that is approximately 4 to 6 days prior to the earthquake. A significant increase of E_p occurred after the earthquake day (March 20-23, 2011). Another significant increment is observed from February 12 to 14 around 39 to 41 km. This increment of E_p may be associated with the earthquake ($M > 5$) which occurred on February 16 in the same region as confirmed by USGS. Figure 5 shows a significant enhancement of E_p at around 34 to 39 km from April 5 to 9, 2012, which occurs 2 to 6 days

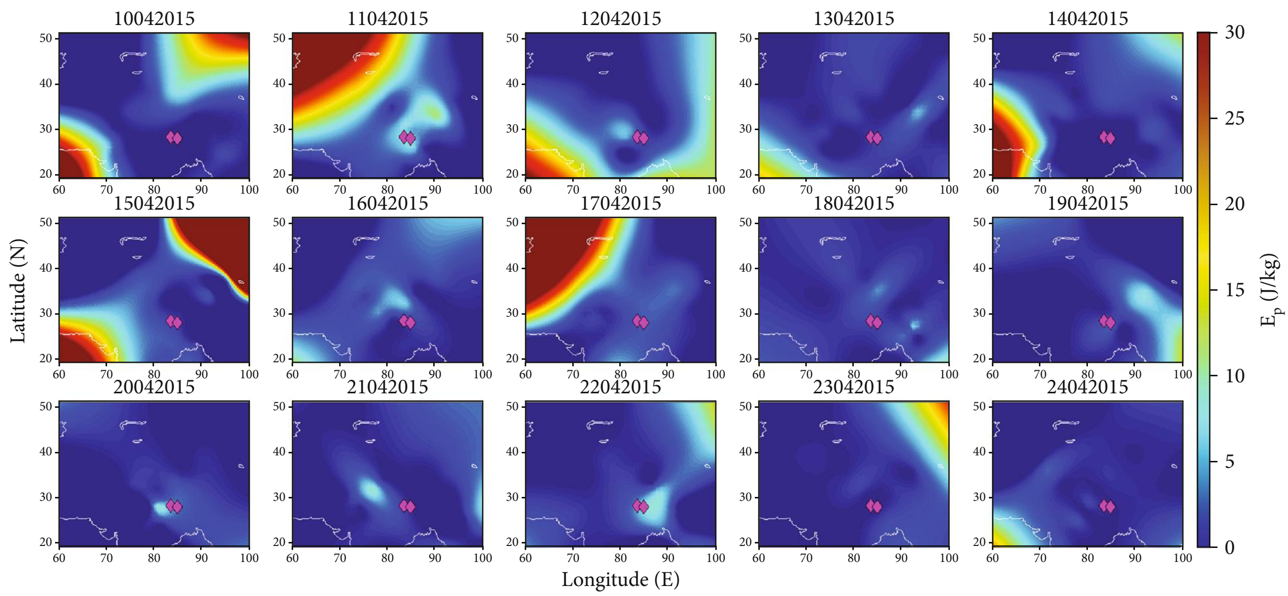

FIGURE 16: Spatial variation of potential energy during April 10 to 24, 2015 for 35 km altitude for Nepal earthquake 2015.

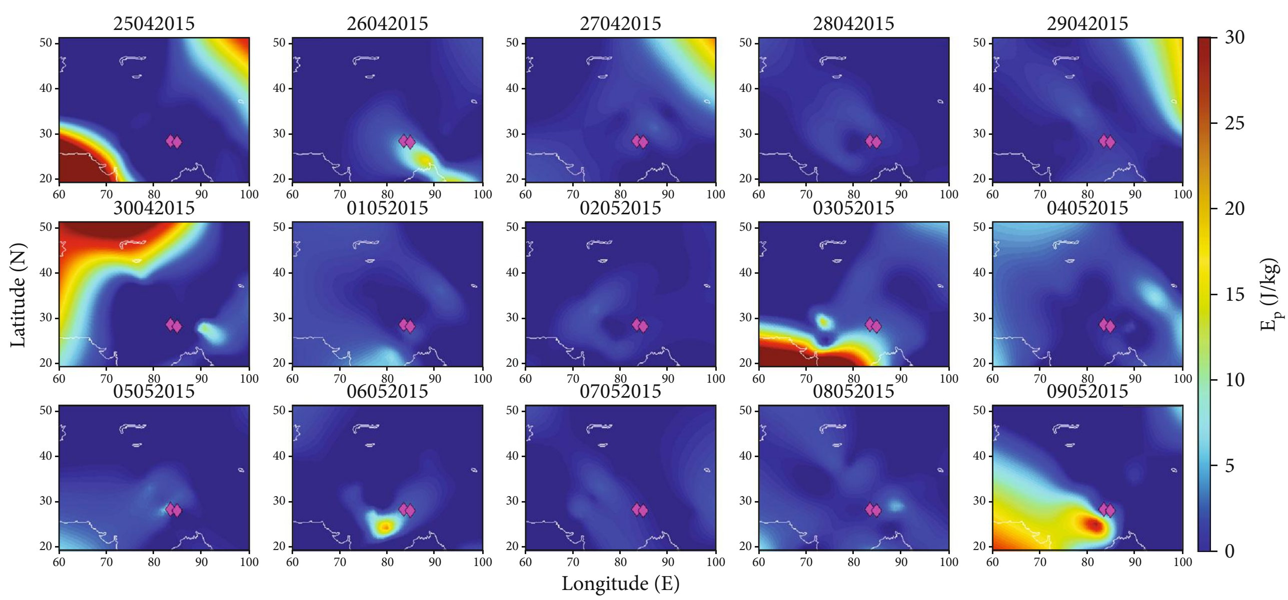

FIGURE 17: Same as Figure 16 from April 25 to May 9, 2015 at 35 km altitude.

prior to the Indian Ocean earthquake. The maximum enhancement occurs on April 8, 2012, which is 3 days prior to the earthquake. Some preenhancements those occurred 18-22 days before the main shock may be related to the earthquakes that occurred around this region with magnitude $M = 5.2$ confirmed by USGS on March 28, 2012, and also contaminated by the equatorial Kelvin waves (KWs). The postenhancements of E_p after the earthquake day around April 14 to 20, 2012 seems like having the contribution from equatorial KWs [54] or can be associated with the aftershocks of the earthquake that occurred on April 15, 2012, with magnitude $M = 6.2$. For the first Nepal earthquake (April 25, 2015), Figure 6 shows enhancement of E_p around 36 to 37 km from April 10 to 12, 2015, approximately 13 to 14 days prior to the event can be considered as a possible preseismic effect. Another enhancement occurs from April 22 to 24, 2015 around 40 to 44 km just 1 to 3 days prior to the earthquake. Some enhancements in E_p are also observed 25-26 days from this earthquake around 46 to 47 km altitude which may be associated to another earthquake that occurred in this region on April 02, 2015, with magnitude $M = 4.9$. From Figure 7, it is observed that a significant

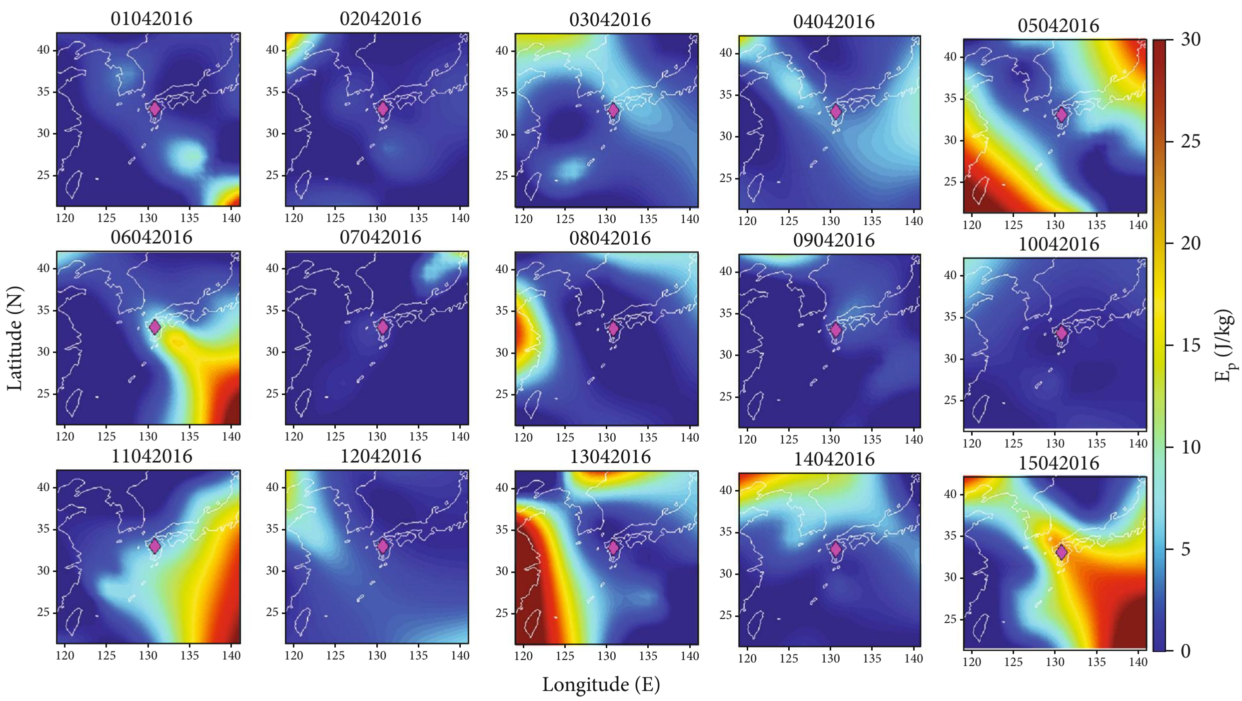

FIGURE 18: Potential energy variation during April 1 to 15, 2016 at 43 km height for Kumamoto Earthquake.

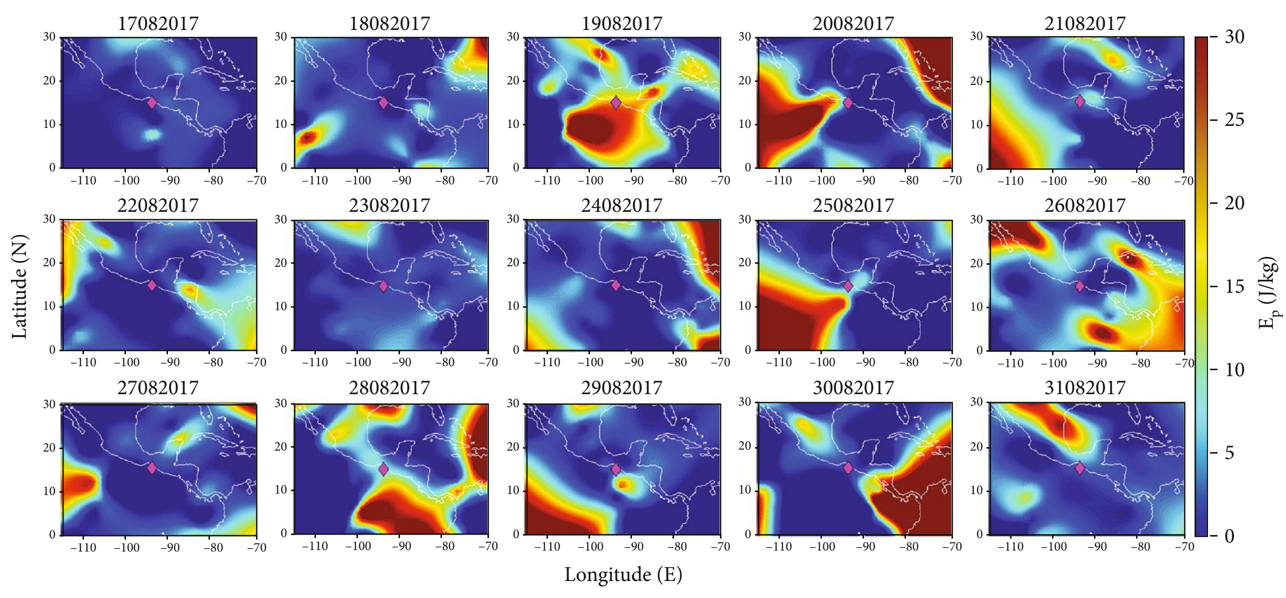

FIGURE 19: Spatial variation of potential energy from August 17 to August 31 at 41 km height for Chiapas earthquake 2017.

amount of E_p enhancement occurs around 34 to 36 km during May 8 to 9, 2015 approximately 3 to 4 days prior to the second Nepal earthquake (May 12, 2015). For the Kumamoto earthquake, Figure 10 shows that the E_p is anomalous increased around 40 to 42 km from April 4 to 6, 2016 about one week prior to the earthquake. For the Chiapas earthquake, there is continuous enhancement occurring before the earthquake. Figure 8 shows that enhancement of E_p is significant around 45 to 48 km during August 17 to 23, 2017. The next enhanced activity is observed around 40 to 42 km from August 23 to 25, 2017. Another enhancement occurs around 41 to 45 km from August 29, 2017, to September 2, 2017. The same effect of equatorial KWs contaminates those seismogenic AGW excitation [69] for the Chiapas earthquake, as it does for the Indian Ocean earthquake (Figure 6).

4.2. Spatial variation of AGWs. After detection of the altitude of maximum the E_p, the main focus is on the spatial variation of E_p over the epicentral region for all the earthquakes. The spatial distributions of E_p around the Tohoku

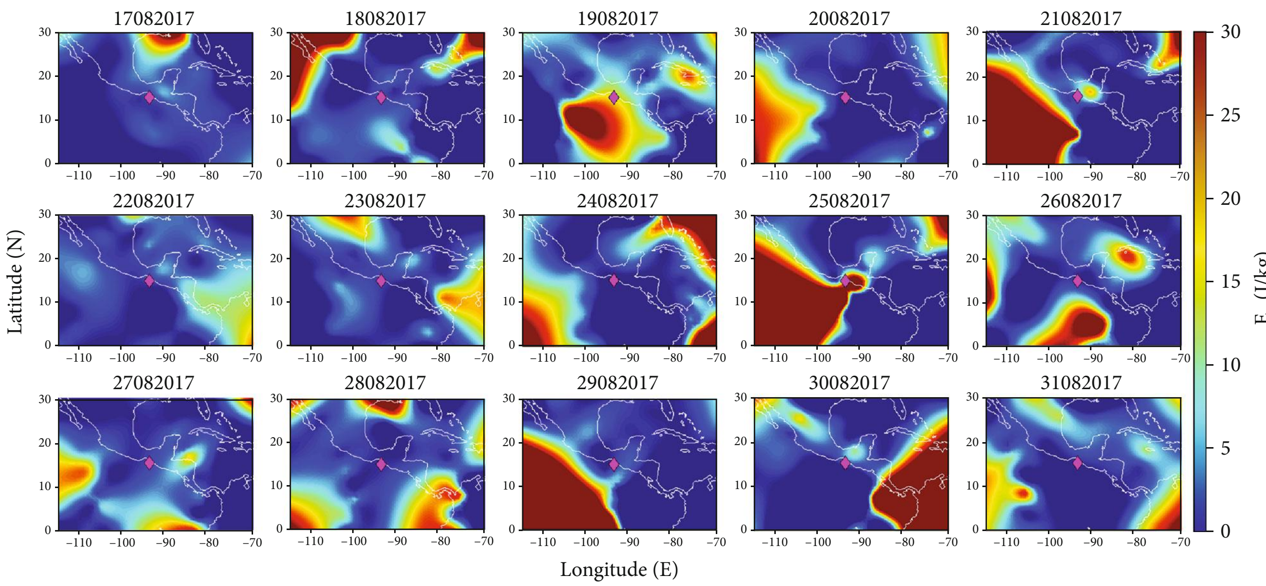

FIGURE 20: Same as Figure 19 from August 17 to August 31 at an altitude of 42 km.

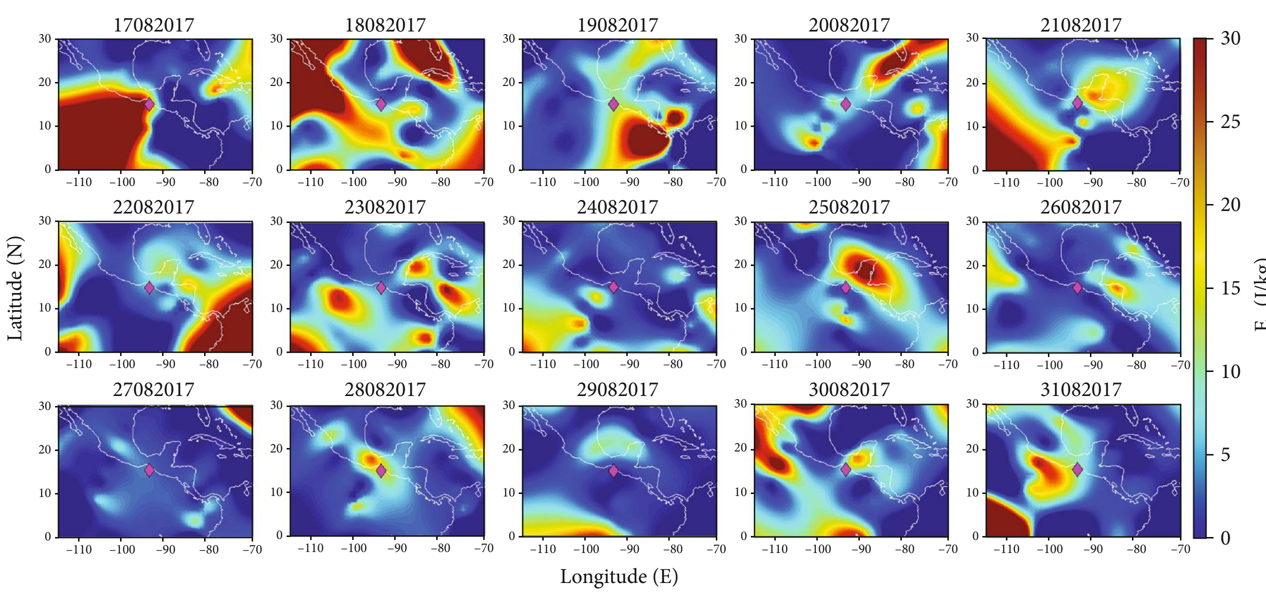

FIGURE 21: Same as Figure 19 from August 17 to August 31 at an altitude of 46 km.

earthquake (February 15, 2011, to March 15, 2011) are shown in Figures 10 and 11. To investigate the spatial distribution, the altitudes of 43 and 44 km are chosen during the Tohoku earthquake. From Figures 10 and 11, it is evident that on February 23 to 24, 2011, there is a tiny patch of potential AGW coupling near the epicenter but the maximum activities are observed on March 5 to 6, 2011 at 43 km. Figure 12 shows that the highly enhanced E_p associated with AGW activity is near the epicentral region on March 4 to 6, 2011 at 44 km with the maximum value observed in observed on March 5, 2011.

For the Indian Ocean earthquake, it is evident from Figures 13–15 (April 01 to 15, 2012) that enhanced E_p is observed near the epicentral region on April 7, 2012, at 34 km, April 8, 2012, at 35 km, April 8 to 12 at 36 km, and April 7, 2012, at 37 km altitude.

For the Nepal earthquakes, A small amount of E_p enhancements was observed near the epicenter on April 20, 2015, and April 22, 2015, at 35 km altitude as shown in Figure 16 (April 10 to May 9, 2015). These enhancements may be associated with the formation of AGW for the first Nepal earthquake on April 26, 2015. Figure 17 reflects a high AGW activity on May 9, 2015, moderate AGW activity on April 26 and May 6, 2015, and a very small AGW activity on May 3, 2015, at 35 km altitude. E_p increments are mainly

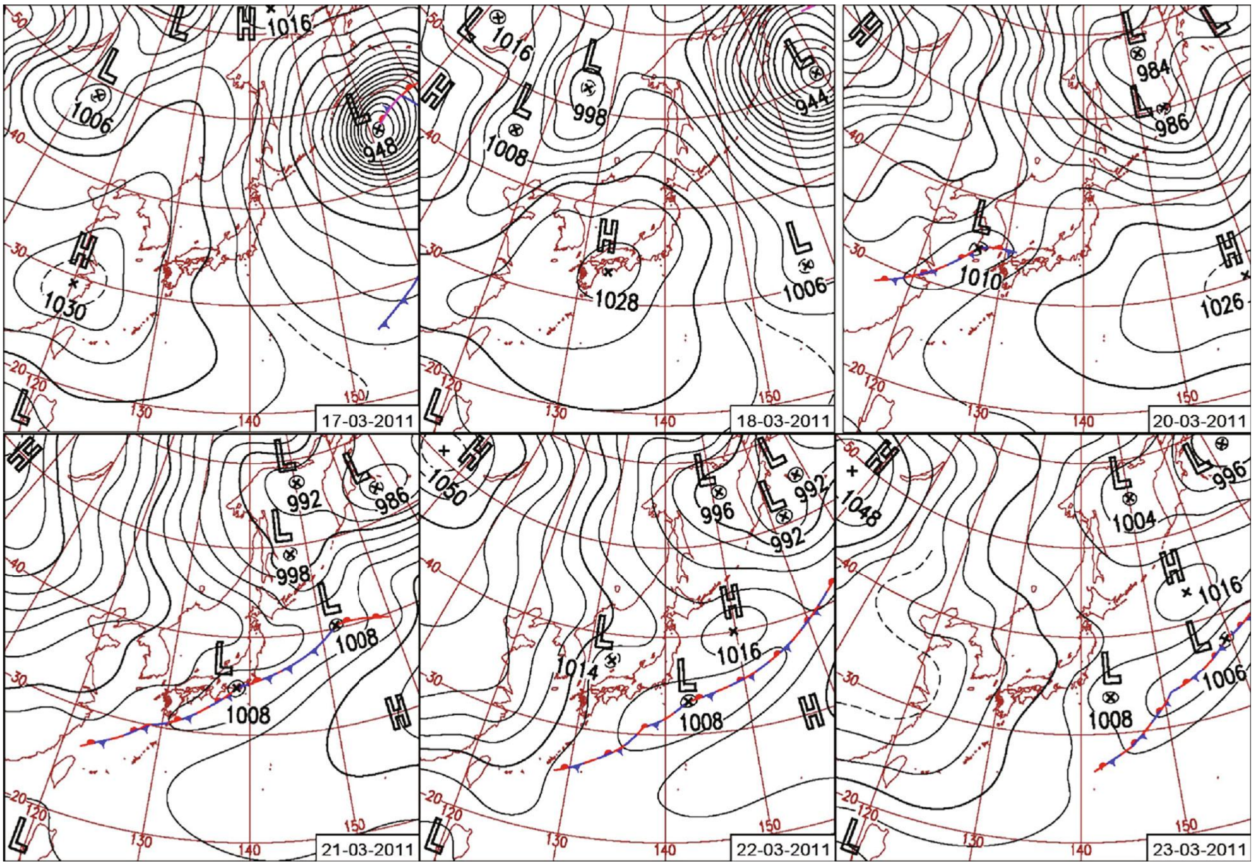

Figure 22: Weather maps during March 17 to 18, and March 20 to 23, 2011 around Japan. The red curve indicates the thunderstorm warning, and blue curve indicates typhoon warning.

due to the possible generation of AGW for the second Nepal earthquake on May 12, 2015.

For Kumamoto earthquake, it is observed that E_p is maximum at the epicentral region on April 6, April 11, and April 15, 2016, at an altitude of 43 km which reflects from the spatial distribution of Figure 18 during April 1 to 15, 2016.

For the Chiapas earthquake, Figure 19 shows that the E_p reaches its maximum value on August 19, 2017, at 41 km altitude and after that, it started to diminish at the epicentral region; again, it is observed on August 25, 2017, around from west direction and scattered around east direction on the next day. The same kind of result is found at 42 km on the same days which are shown in Figure 20. From Figure 21, it is evident that the enhancements in E_p is maximum during August 17 to 18, 21 to 25, 28, and 30 to 31, 2017 at 46 km near the epicentral region.

5. Discussions

In this manuscript, the study is mainly focused on preseismic activity of AGW before four great earthquakes and three major earthquakes. It is evident from Figures 4 and 8 that there is evidence of enhancement in E_p after the Tohoku and Kumamoto earthquake. For the Tohoku earthquake, the possible generation of AGWs during March 20-23, 2011, is not generated due to a geomagnetic storm on March 21, 2011. The formation of the AGWs is directly connected to the cyclones. A possible mechanism for the increment is the activities of cyclonic systems around 45°–60°N. On March 20, there were three cyclonic (low pressure) systems throughout the Sea of Okhotsk and the Kamchatka Peninsula. All of them were the remnants of an Aleutian Low peaked on March 17 to 18. The front and low pressure were approaching from the west on March 20, and it is very near to the southern region of the Tohoku state on March 21 and then approaching towards the east during March 22-23, 2011. The weather maps are taken from the Japan Meteorological Agency (JMA) as shown in Figure 22. Convective systems usually exist around cyclones causing AGWs. In a similar way, for the Kumamoto earthquake, the enhancement of E_p on the earthquake day is not generated due to the geomagnetic storm that occurred on the earthquake day. It is mainly formed due to a few frontal systems accompanied cyclones passed the studied region (20°-30°N, 120°-140°E) during April 14 to 19, 2016 shown in the weather maps (Figure 23).

In spatial variation of AGW, the huge patches seen in Figures 11–21 are mostly the result of synoptic and planetary-scale (hundreds to thousands of kilometers) meteorological systems. These systems can cause disturbances in

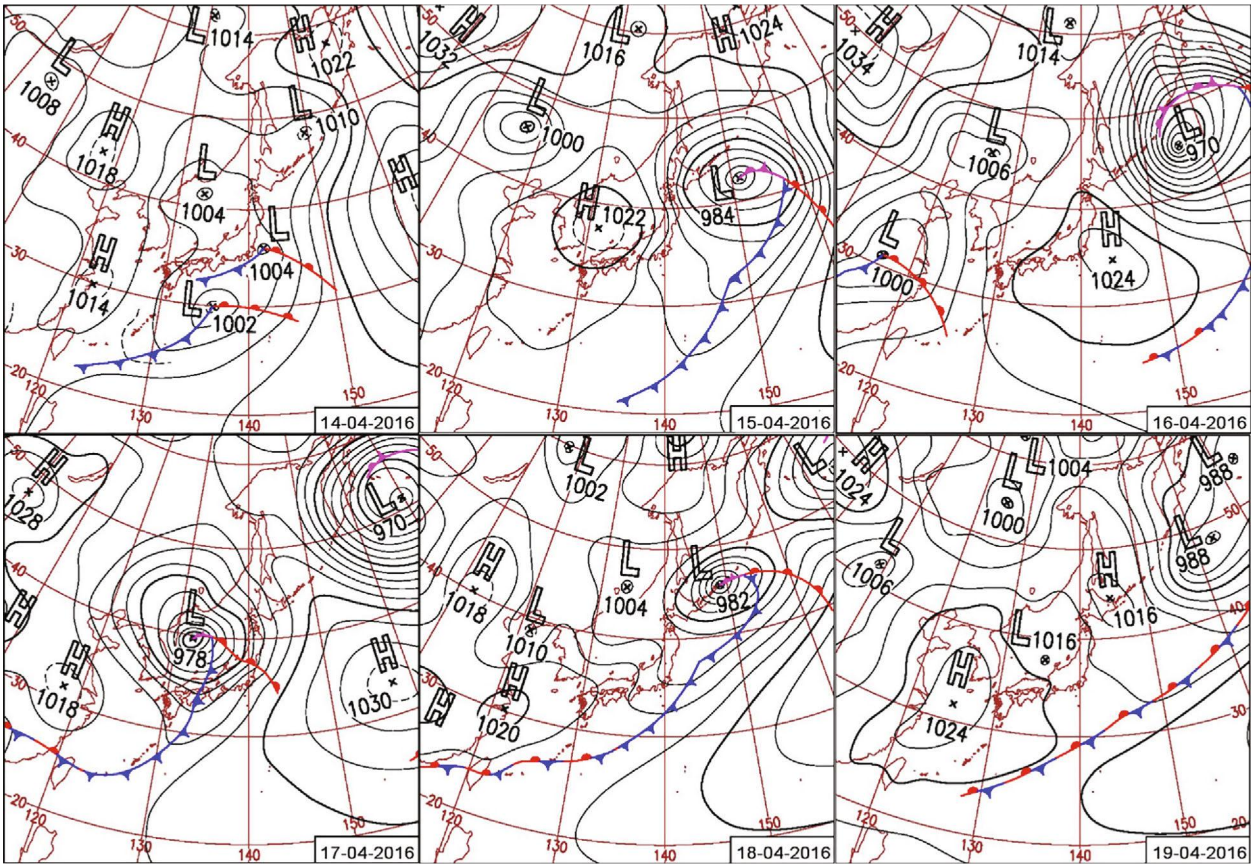

Figure 23: Weather maps during April 14 to 19, 2016 around Japan. Figure format similar to Figure 22.

the atmosphere and either move fast eastward or westward. As a result, they generate wide-scale temperature fluctuations, resulting in huge patches of high E_p region, as seen in these figures.

6. Conclusions

As reported by various researchers in recent years, the possibility of AGWs playing a significant role in detecting preseismic disturbances is indeed a well-proven phenomenon [7, 8]. AGW is one of the regulating agents in the acoustics channel of the LAIC mechanism, which originates from pressure or temperature convection caused by seismogenic sources. This manuscript elaborately discusses such phenomena based on a space-based observation. An indirect approach is used to detect this AGW operation from the principle of convective currents throughout the lower stratosphere since there is no clear way to classify the excitation of AGW in the stratosphere before earthquakes. SABER/TIMED temperature profile is used to calculate the E_p associated with such AGW in this manuscript. We focused on four great and three major earthquakes occurred at various periods and in various geographical regions around the world. The spatiotemporal patterns of potential energy are investigated for these seven earthquakes that occurred in Tohoku, the Indian Ocean, Nepal, Kumamoto, and Chiapas.

For the Tohoku earthquake (March 11, 2011), AGW excitation in a form of potential energy enhancement is observed at 43 km altitude and on 4 to 6 days prior to the earthquake day. For the Indian Ocean earthquake (April 11, 2012), similar AGW activity became maximum on 2 to 6 days prior to the days of the earthquake at 34 to 37 km altitude. For the Nepal earthquake, the preseismic irregularities started a bit earlier. The first AGW activity has been detected on 13 to 14 days before the day of the first Nepal earthquake (April 25, 2015) at 35 to 36 km altitude, and another enhancement has been identified on 1 to 3 days prior to the day of the same earthquake at an altitude 40 to 42 km. For the second Nepal earthquake (May 12, 2015), an enhancement of potential energy associated with AGW has been observed on 3 to 4 days prior the earthquake day at an altitude of 34 to 36 km. For the Kumamoto earthquake (April 15, 2016), at a height of 43 km, AGW activity has been detected, on 8 to 9 days prior to the earthquake day. At an altitude of 42 to 46 km, the anomalous increase in E_p correlated with AGW was observed one week prior to the Chiapas earthquake (September 8, 2017). Some postearthquake AGW activity has been observed for the Tohoku and the Kumamoto earthquakes. These anomalies due to typhoons and cyclones over the Japan region are reported during the same time frame and responsible to generate such wave-like phenomena. The equatorial KWs also play a vital role in AGW excitation [69] Significant enhancement in E_p has been observed after the main shock for the Indian Ocean earthquake as it happened near the equatorial region. For the Chiapas earthquake, a similar contribution from equatorial KWs possibly contaminated the result.

According to JMA, no cyclones or convective systems were formed in the 15 days prior to the 2011 Tohoku earthquake. From March 21 to 23, many cyclonic systems emerged at 45°–60°N in the postearthquake period. In this study, for Tohoku earthquake, the maximum enhancement of E_p is observed before the earthquake around March 05 to 07, 2011. As no cyclones occurred during that time frame, the increased AGW activity may have been caused by the earthquake. The postenhancement of E_p between March 21 and 23 was caused by the formation of cyclonic systems in that region. There were no cyclonic systems formed in the pre-earthquake timeframe, according to Bureau of Meteorology reports of March and April 2012. From April 16 to 25, 2012, a postearthquake low pressure area (classified as 19 U) was developed in Australia, with the lowest pressure of 1006 hPa. In our observation, the highest enhancement of E_p is observed before the earthquake around April 5 to 9, 2012 and since the period is meteorologically and geomagnetically quiet, the generation of AGW is possibly connected to the earthquake. The postenhanced activity of AGW may be connected to that low pressure formation around Australia or may be due to contamination of KWs and aftershocks of the earthquake. According to weather report of April and May from IMD, no cyclones were formed between the chosen pre- and post-earthquake period around that region for both Nepal earthquakes. Since the period was meteorologically as well as geomagnetically quiet, the enhanced activity of AGW around April 22-24 and May 09, 2015, may be connected to earthquake. According to the JMA weather report for April 2016, no cyclonic systems were formed before the earthquake; however, cyclonic activity was reported in the selected region from March 14 to 19, 2016. From the observation, the enhanced AGW activity is observed around April 4 to 6, 2016. The activity may be linked to the earthquake because the time is free of all kinds of meteorological phenomena and geomagnetically quiet. The other enhancements around April 14 to 19 may be connected to the cyclonic system around the region. According to NWS and NOAA reports, the preearthquake period was meteorologically quiet and free from any kind of cyclone or convective systems but a major hurricane Irma passed around 20°N to 25°N and -70°W to 85°W within spatial area chosen for Chiapas earthquake from September 07 to 09, 2017. Another major hurricane Katia also passed through the chosen area around 22°N to 25°N and 94°W to 98°W from September 05 to 09, 2017. Though the periods August 17–19 and August 31–September 2 were meteorologically quiet with solar activities, Sasmal et al. [22] and Biswas et al. [43] have demonstrated that the geomagnetic storm has a contaminating impact in the electromagnetic channel of LAIC but not in the acoustic channel, implying that AGW activity may be unaffected. So, the observed activity is possibly connected to the earthquake. The period from August 24 to 28 was absolutely solar quiet; so, the enhanced activity of AGW is possibly connected to earthquake.

The observed outcomes are compared with the previously detected AGWs for the same earthquake. The study of Yang et al. [51] used ERA5 reanalysis data for the investigation of AGW activity for the Kumamoto earthquake and presented a similar increase in AGW activity 4 to 6 days prior to the earthquake. In SABER observation, similar kind of results both in the temporal and spatial measurements is identified. In another work by Yang et al. [49] for 2011, the Tohoku earthquake is also verified by the observation through SABER. Wave-like structure in the range of AGW has been detected previously in a different way by Chakraborty et al. [9] where the computation of AGW has been achieved by taking the wavelet of nighttime VLF signal during Nepal earthquake. A significant enhancement of AGW 3 days before the second Nepal earthquake (May 12, 2015) is observed in Chakraborty et al. [9]. Very recently, Biswas et al. [43] also compared the AGW enhancement both observed from night-time VLF fluctuation as well as SABER observation for a separate earthquake in Imphal, India, on January 3, 2016 (UT) where the identical spatiotemporal effect has been unidentified. Thus, the observation of this study through a new methodology is consistent with the previous works and, for most of the cases, the AGW enhancement is preseismic in nature. As the physical mechanism behind the LAIC is still under investigation, this study needs much attention. In contrast to earlier works, this works dealt with a large number of earthquakes for investigating such AGW phenomena. As, in most cases, there are no such huge space weather phenomena that happened before the earthquakes, and these AGW activities are mostly due to the seismogenic sources. To testify these preseismic AGW variations as a key ingredient of the acoustics channel of LAIC, other parameters from thermal (surface latent heat flux, relative humidity, etc.) and electromagnetic channel (VLF radio anomalies, total electron content (TEC) anomalies, energetic particle precipitation, etc.) are being thoroughly analyzed separately and will be reported elsewhere as a multiparametric study of LAIC phenomena.

Data Availability

The data of atmospheric temperature is taken from the SABER data archive (http://saber.gats-inc.com/), the geomagnetic data is taken from OMNIWEB NASA Archive, and the earthquake regarding information is taken from USGS.

Disclosure

This paper is focused on SABER satellite observations of the precursory effect for massive earthquakes in stratospheric atmospheric gravity wave (AGW).

Conflicts of Interest

We have no conflicts of interest to disclose.

Acknowledgments

The authors are grateful for financial assistance from the DST-INSPIRE fellowship (IF170010 & IF170619), the DST-SERB (EMR/2016/003889) fellowship, and the Government of West Bengal. SABER and their research staff, as well as NASA OMNIWEB, are to be commended for presenting scientific evidence. For scientific assistance, we thank Japan Trust, the National Institute of Information and Communication Technology (NICT), and the Hayakawa Institute of Seismo-Electromagnetis Co., Ltd. (Hi-SEM). We also thank the Japan Meteorological Agency for providing Japan's weather maps.

References

[1] O. A. Molchanov and M. Hayakawa, *Seismo Electromagnetics and Related Phenomena: History and latest results*, TERRAPUB, Tokyo, 2008.

[2] O. A. Molchanov, *Lithosphere-atmosphere-ionosphere coupling due to seismicity*, Transworld Research Network, Trivandrum(India), 2009.

[3] S. A. Pulinets and D. Ouzounov, "Lithosphere-atmosphere-ionosphere coupling (LAIC) model - an unified concept for earthquake precursors validation," *Journal of Asian Earth Sciences*, vol. 41, no. 4-5, pp. 371–382, 2011.

[4] M. Hayakawa, O. A. Molchanov, T. Ondoh, and E. Kawai, "The precursory signature effect of the Kobe earthquake on VLF subionospheric signals," *Journal of the Communications Research Laboratory*, vol. 43, no. 2, pp. 169–180, 1996.

[5] M. A. Clilverd, C. J. Rodger, and N. R. Thomson, "Investigating seismoionospheric effects on a long subionospheric path," *Journal of Geophysical Research*, vol. 104, no. A12, pp. 28171–28179, 1999.

[6] Y. Hobara and M. Parrot, "Ionospheric perturbations linked to a very powerful seismic event," *Journal of Atmospheric and Solar-Terrestrial Physics*, vol. 67, no. 7, pp. 677–685, 2005.

[7] M. Hayakawa, Y. Kasahara, T. Nakamura et al., "Atmospheric gravity waves as a possible candidate for seismo-ionospheric perturbations," *Journal of Atmospheric Electricity*, vol. 31, no. 2, pp. 129–140, 2011.

[8] M. Hayakawa, T. Asano, A. Rozhnoi, and M. Solovieva, "VLF/LF Sounding of Ionospheric Perturbations and Possible Association with Earthquakes," in *Pre-Earthquake Processes: A Multi-Disciplinary Approach to Earthquake Prediction Studies*, D. Ouzounov, S. Pulinets, K. Hattori, and P. Taylor, Eds., pp. 277–304, American Geophysical Union, Washington DC, 2018.

[9] S. Chakraborty, S. Sasmal, S. K. Chakrabarti, and A. Bhattacharya, "Observational signatures of unusual outgoing longwave radiation (OLR) and atmospheric gravity waves (AGW) as precursory effects of May 2015 Nepal earthquakes," *Journal of Geodynamics*, vol. 113, pp. 43–51, 2018.

[10] S. Sasmal, "Renaissance of VLF Science in Indian Context," *Astrophysics and Space Science Proceedings*, vol. 53, pp. 513–525, 2018.

[11] D. Z. Politis, S. M. Potirakis, Y. F. Contoyiannis, S. Biswas, S. Sasmal, and M. Hayakawa, "Statistical and criticality analysis of the lower ionosphere prior to the 30 October 2020 Samos (Greece) Earthquake (M6.9), based on VLF electromagnetic propagation data as recorded by a new VLF/LF receiver installed in Athens (Greece)," *Entropy*, vol. 23, no. 6, p. 676, 2021.

[12] A. Y. Schekotov, O. A. Molchanov, M. Hayakawa et al., "ULF/ELF magnetic field variations from atmosphere induced by seismicity," *Radio Science*, vol. 42, article RS6S90, no. 6, 2007.

[13] M. Parrot, "Statistical analysis of the ion density measured by the satellite DEMETER in relation with the seismic activity," *Earthquake Science*, vol. 24, no. 6, pp. 513–521, 2011.

[14] S. Ghosh, S. Sasmal, S. Midya, and S. K. Chakrabarti, "Unusual change in critical frequency of F_2; layer during and prior to earthquakes," *Open Journal of Earthquake Research*, vol. 6, no. 4, pp. 191–203, 2017.

[15] J. Y. Liu, C. Y. Chen, Y. Y. Sun, I. T. Lee, and J. Chum, "Fluctuations on vertical profiles of the ionospheric electron density perturbed by the March 11, 2011 M9.0 Tohoku earthquake and tsunami," *GPS Solutions*, vol. 23, no. 3, p. 76, 2019.

[16] J. Y. Liu, Y. I. Chen, Y. J. Chuo, and H. F. Tsai, "Variations of ionospheric total electron content during the Chi-Chi earthquake," *Geophysical Research Letters*, vol. 28, no. 7, pp. 1383–1386, 2001.

[17] E. L. Afraimovich, E. I. Astafieva, M. B. Gokhberg et al., ""Variations of the total electron content in the ionosphere from GPS data recorded during the Hector Mine earthquake of October 16, 1999", California," *Russian Journal of Earth Sciences*, vol. 6, no. 5, pp. 339–354, 2004.

[18] J. Y. Liu, Y. J. Chuo, S. J. Shan et al., "Pre-earthquake ionospheric anomalies registered by continuous GPS TEC measurements," *Annales de Geophysique*, vol. 22, no. 5, pp. 1585–1593, 2004.

[19] J. Y. Liu, Y. I. Chen, Y. J. Chuo, and C. S. Chen, "A statistical investigation of preearthquake ionospheric anomaly," *Journal of Geophysical Research*, vol. 111, no. A5, article A05304, 2006.

[20] M. Piersanti, M. Materassi, R. Battiston et al., "Magnetospheric–ionospheric–lithospheric coupling model. 1: observations during the 5 August 2018 Bayan Earthquake," *Remote Sensing*, vol. 12, no. 20, p. 3299, 2020.

[21] Y. Zhang, X. Liu, J. Guo, K. Shi, M. Zhou, and F. Wang, "Coseismic ionospheric disturbance with Alaska strike-slip Mw7.9 erthquake on 23 January 2018 monitored by GPS," *Atmosphere*, vol. 12, no. 1, p. 83, 2021.

[22] S. Sasmal, S. Chowdhury, S. Kundu et al., "Pre-seismic irregularities during the 2020 Samos (Greece) earthquake (M = 6.9) as investigated from multi-parameter approach by ground and space-based techniques," *Atmosphere*, vol. 12, no. 8, p. 1059, 2021.

[23] O. M. Phillips, "On the generation of waves by turbulent wind," *Journal of Fluid Mechanics*, vol. 2, no. 5, pp. 417–445, 1957.

[24] J. Lighthill, *Waves in fluids*, vol. 205, Cambridge University Press, 2001.

[25] D. C. Fritts and M. J. Alexander, "Gravity wave dynamics and effects in the middle atmosphere," *Reviews of Geophysics*, vol. 41, no. 1, p. 1003, 2003.

[26] T. P. Lane, R. D. Sharman, T. L. Clark, and H. M. Hsu, "An investigation of turbulence generation mechanisms above deep convection," *Journal of the Atmospheric Sciences*, vol. 60, no. 10, pp. 1297–1321, 2003.

[27] B. E. Mapes, "Gregarious tropical convection," *Journal of the Atmospheric Sciences*, vol. 50, no. 13, pp. 2026–2037, 1993.

[28] T. P. Lane and R. D. Sharman, "Gravity wave breaking, secondary wave generation, and mixing above deep convection

in a three-dimensional cloud model," *Geophysical Research Letters*, vol. 33, no. 23, p. L23813, 2006.

[29] Y. I. Galperin and M. Hayakawa, "On the magnetospheric effects of experimental ground explosions observed from aureol-3," *Journal of Geomagnetism and Geoelectricity*, vol. 48, no. 10, pp. 1241–1263, 1996.

[30] V. Carbone, M. Piersanti, M. Materassi, R. Battiston, F. Lepreti, and P. Ubertini, "A mathematical model of lithosphere-atmosphere coupling for seismic events," *Scientific Reports*, vol. 11, no. 1, p. 8682, 2021.

[31] S. V. Garmash, E. N. Lin'kov, L. N. Petrova, and G. N. Shved, "Excitation of atmo- spheric oscillations by seismogravitational vibrations of the earth," *Izvestiya AN USSR Fizika Atmosfery i Okeana*, vol. 35, pp. 1290–1299, 1989.

[32] E. M. Linkov, L. N. Petrova, and D. D. Zuroshvili, "Seismogravitational vibrations of the earth and related disturbances of the atmosphere," *Doklady Akademii Nauk SSSR*, vol. 306, pp. 315–317, 1989.

[33] S. L. Shalimov, "Lithosphere-ionosphere relationship: A new way to predict earthquakes?," *Episodes International Geophysics Newsmagazine*, vol. 15, pp. 252–254, 1992.

[34] Y. Murayama, T. Tsuda, and S. Fukao, "Seasonal variation of gravity wave activity in the lower atmosphere observed with the MU radar," *Journal of Geophysical Research – Atmospheres*, vol. 99, no. D11, pp. 23057–23069, 1994.

[35] T. Tsuda, Y. Murayama, T. Nakamura et al., "Variations of the gravity wave characteristics with height, season and latitude revealed by comparative observations," *Journal of Atmospheric and Terrestrial Physics*, vol. 56, no. 5, pp. 555–568, 1994.

[36] T. Tsuda, M. Nishida, C. Rocken, and R. H. Ware, "A global morphology of gravity wave activity in the stratosphere revealed by the GPS occultation data (GPS/MET)," *Journal of Geophysical Research: Atmospheres*, vol. 105, no. D6, pp. 7257–7273, 2000.

[37] S. K. Dhaka, P. K. Devrajan, Y. Shibagaki, R. K. Choudhary, and S. Fukao, "Indian MST radar observations of gravity wave activities associated with tropical convection," *Journal of Atmospheric and Solar-Terrestrial Physics*, vol. 63, no. 15, pp. 1631–1642, 2001.

[38] S. K. Dhaka, R. K. Choudhary, S. Malik, Y. Shibagaki, M. D. Yamanaka, and S. Fukao, "Observable signatures of a convectively generated wave field over the tropics using Indian MST radar at Gadanki (13.5 ° N, 79.2 ° E)," *Geophysical Research Letters*, vol. 29, no. 18, pp. 19-1–19-4, 2002.

[39] K. Miyaki, M. Hayakawa, and O. A. Molchanov, *The role of gravity waves in the lithosphere-ionosphere coupling, as revealed from the subionospheric LF propagation data in Seismo-Electromagnetics, Lithosphere-Atmosphere-Ionosphere Coupling*, Terrapub, Tokyo, 2002.

[40] V. Korepanov, M. Hayakawa, Y. Yampolski, and G. Lizunov, "AGW as a seismo-ionospheric coupling responsible agent," *Physics and Chemistry of the Earth, Parts A/B/C*, vol. 34, no. 6-7, pp. 485–495, 2009.

[41] Y. Zhang, J. Xiong, L. Liu, and W. Wan, "A global morphology of gravity wave activity in the stratosphere revealed by the 8-year SABER/TIMED data," *Journal of Geophysical Research: Atmospheres*, vol. 117, no. D21, p. D21101, 2012.

[42] T. Nakamura, V. Korepanov, Y. Kasahara, Y. Hobara, and M. Hayakawa, "An evidence on the lithosphere-ionosphere coupling in terms of atmospheric gravity waves on the basis of a combined analysis of surface pressure, ionospheric perturbations and ground-based ULF variations," *Journal of Atmospheric Electricity*, vol. 33, no. 1, pp. 53–68, 2013.

[43] S. Biswas, S. Kundu, S. Ghosh et al., "Contaminated effect of geomagnetic storms on pre-seismic atmospheric and ionospheric anomalies during Imphal earthquake," *Open Journal of Earthquake Research*, vol. 9, no. 5, pp. 383–402, 2020.

[44] D. Ouzounov, S. Pulinets, A. Romanov et al., "Atmosphere-ionosphere response to the M9 Tohoku earthquake revealed by multi-instrument space-borne and ground observations: Preliminary results," *Earthquake Science*, vol. 24, no. 6, pp. 557–564, 2011.

[45] H. Ohta, J. Izutsu, A. Schekotov, and M. Hayakawa, "The ULF/ELF electromagnetic radiation before the 11 March 2011 Japanese earthquake," *Radio Science*, vol. 48, no. 5, pp. 589–596, 2013.

[46] S. Sasmal, S. K. Chakrabarti, and S. Ray, "Unusual behavior of very low frequency signal during the earthquake at Honshu/Japan on 11 March, 2011," *Indian Journal of Physics*, vol. 88, no. 10, pp. 1013–1019, 2014.

[47] A. Schekotov, H. J. Zhou, X. L. Qiao, and M. Hayakawa, "ULF/ELF atmospheric radiation in possible association to the 2011 Tohoku earthquake as observed in China," *Earth Sciences Research*, vol. 5, no. 2, p. 47, 2016.

[48] S. Ghosh, S. Chakraborty, S. Sasmal, T. Basak, S. K. Chakrabarti, and A. Samanta, "Comparative study of the possible lower ionospheric anomalies in very low frequency (VLF) signal during Honshu, 2011 and Nepal, 2015 earthquakes," *Geomatics, Natural Hazards and Risk*, vol. 10, no. 1, pp. 1596–1612, 2019.

[49] S. S. Yang and M. Hayakawa, "Gravity wave activity in the stratosphere before the 2011 Tohoku earthquake as the mechanism of lithosphere-atmosphere- ionosphere coupling," *Entropy*, vol. 22, no. 1, p. 110, 2020.

[50] S. Chakraborty, S. Sasmal, T. Basak et al., "Numerical modeling of possible lower ionospheric anomalies associated with Nepal earthquake in May, 2015," *Advances in Space Research*, vol. 60, no. 8, pp. 1787–1796, 2017.

[51] M. Shah, M. Khan, K. Ullah, and S. Ali, "Thermal anomalies prior to The 2015 Gorkha (Nepal) earthquake from modis land surface temperature and outgoing longwave radiations," *Geodynamics & Tectonophysics*, vol. 9, no. 1, pp. 123–138, 2018.

[52] S. S. Yang, T. Asano, and M. Hayakawa, "Abnormal gravity wave activity in the stratosphere prior to the 2016 Kumamoto earthquakes," *Journal of Geophysical Research: Space Physics*, vol. 124, pp. 1410–1425, 2019.

[53] T. Hu, Y. Yao, and J. Kong, "Study of spatial and temporal variations of ionospheric total electron content in Japan, during 2014–2019 and the 2016 Kumamoto earthquake," *Sensors*, vol. 21, no. 6, p. 2156, 2021.

[54] D. A. Stănică and D. Stănică, "ULF pre-seismic geomagnetic anomalous signal related to Mw8.1 offshore Chiapas earthquake, Mexico on 8 September 2017," *Entropy*, vol. 21, no. 1, p. 29, 2019.

[55] K. Shi, H. Ding, J. Guo, and T. Yu, "Refined seismic-ionospheric effects: case study of Mw 8.2 Chiapas earthquake on September 7, 2017," *GPS Solutions*, vol. 25, no. 3, p. 87, 2021.

[56] I. P. Dobrovolsky, S. I. Zubkov, and V. I. Miachkin, "Estimation of the size of earthquake preparation zones," *PAGEOPH*, vol. 117, no. 5, pp. 1025–1044, 1979.

[57] J. M. Russell, M. G. Mlynczak, L. L. Gordley, J. Tansock, and R. Esplin, "An overview of the SABER experiment and preliminary calibration results," *Proceedings of SPIE The International Society for Optical Engineering*, vol. 3756, pp. 277–288, 1999.

[58] J. Shuai, S. D. Zhang, C. M. Huang et al., "Climatology of global gravity wave activity and dissipation revealed by SABER/TIMED temperature observations," *Science China Technological Sciences*, vol. 57, no. 5, pp. 998–1009, 2014.

[59] E. E. Remsberg, B. T. Marshall, M. Garcia-Comas et al., "Assessment of the quality of the version 1.07 temperature-versus-pressure profiles of the middle atmosphere from TIMED/SABER," *Journal of Geophysical Research*, vol. 113, no. D17, p. D17101, 2008.

[60] P. Preusse, A. Dörnbrack, S. D. Eckermann et al., "Space-based measurements of stratospheric mountain waves by CRISTA 1. Sensitivity, analysis method, and a case study," *Journal of Geophysical Research*, vol. 107, no. D23, pp. CRI 6-1–CRI 6-23, 2002.

[61] E. J. Fetzer and J. C. Gille, "Gravity wave Variance in LIMS temperatures. Part I: Variability and comparison with background winds," *Journal of the Atmospheric Sciences*, vol. 51, no. 17, pp. 2461–2483, 1994.

[62] P. Preusse, S. D. Eckermann, M. Ern et al., "Global ray tracing simulations of the SABER gravity wave climatology," *Journal of Geophysical Research*, vol. 114, no. D8, p. D08126, 2009.

[63] X. Yan, N. Arnold, and J. Remedios, "Global observations of gravity waves from High Resolution Dynamics Limb Sounder temperature measurements: a yearlong record of temperature amplitude and vertical wavelength," *Journal of Geophysical Research*, vol. 115, no. D10, p. D10113, 2010.

[64] C. Yamashita, S. L. England, T. J. Immel, and L. C. Chang, "Gravity wave variations during elevated stratopause events using SABER observations," *Journal of Geophysical Research – Atmospheres*, vol. 118, pp. 5297–5306, 2013.

[65] B. Thurairajah, S. M. Bailey, C. Y. Cullens, M. E. Hervig, and J. M. Russell III, "Gravity wave activity during recent stratospheric sudden warming events from SOFIE temperature measurements," *Journal of Geophysical Research – Atmospheres*, vol. 119, no. 13, pp. 8091–8103, 2014.

[66] S. S. Yang, C. J. Pan, U. Das, and H. C. Lai, "Analysis of synoptic scale controlling factors in the distribution of gravity wave potential energy," *Journal of Atmospheric and Solar-Terrestrial Physics*, vol. 135, pp. 126–135, 2015.

[67] X. Liu, J. Yue, J. Xu et al., "Variations of global gravity waves derived from 14 years of SABER temperature observations," *Journal of Geophysical Research: Atmospheres*, vol. 122, no. 12, pp. 6231–6249, 2017.

[68] X. Liu, J. Xu, J. Yue, S. L. Vadas, and E. Becker, "Orographic primary and secondary gravity waves in the middle atmosphere from 16-year SABER observations," *Geophysical Research Letters*, vol. 46, no. 8, pp. 4512–4522, 2019.

[69] D. Nath, W. Chen, and A. Guharay, "Climatology of stratospheric gravity waves and their interaction with zonal mean wind over the tropics using GPS RO and ground-based measurements in the two phases of QBO," *Theoretical and Applied Climatology*, vol. 119, no. 3-4, pp. 757–769, 2015.